# A Coordinated Microstructural and Isotopic Study of a Wark-Lovering Rim on a Vigarano CAI

Jangmi Han[a,b,*], Lindsay P. Keller[b], Ming-Chang Liu[c], Andrew W. Needham[a,b], Andreas T. Hertwig[c], Scott Messenger[b], and Justin I. Simon[b]

[a] Lunar and Planetary Institute, USRA, 3600 Bay Area Boulevard, Houston, TX 77058, USA

[b] Astromaterials Research and Exploration Science, NASA Johnson Space Center, Houston, TX 77058, USA

[c] Department of Earth, Planetary, and Space Sciences, University of California, Los Angeles, Los Angeles, CA 90095, USA

*Corresponding author at: Lunar and Planetary Institute & NASA Johnson Space Center, Houston, TX, 77058, USA. E-mail address: han@lpi.usra.edu (J. Han).

Submitted to *Geochimica et Cosmochimica Acta*

March 08, 2019

Revised October 08, 2019

## ABSTRACT

We carried out a coordinated mineralogical and isotopic study of a Wark-Lovering (WL) rim on a Ca,Al-rich inclusion (CAI) from the reduced CV3 chondrite Vigarano. The outermost edge of the CAI mantle is mineralogically and texturally distinct compared to the underlying mantle that is composed of coarse, zoned melilite ($Åk_{\sim 10\text{-}60}$) grains. The mantle edge contains fine-grained gehlenite with hibonite and rare grossite that likely formed by rapid crystallization from a melt enriched in Ca and Al. These gehlenite and hibonite layers are surrounded by successive layers of spinel, zoned melilite ($Åk_{\sim 0\text{-}10}$), zoned diopside that grades outwards from Al,Ti-rich to Al,Ti-poor, and forsteritic olivine intergrown with diopside. These layered textures are indicative of sequential condensation of spinel, melilite, diopside, and forsterite onto hibonite. Anorthite occurs as a discontinuous layer that corrodes adjacent melilite and Al-

diopside, and appears to have replaced them, probably even later than the forsterite layer formation. Based on these observations, we conclude that the WL rim formation was initiated by flash melting and extensive evaporation of the original inclusion edge, followed by subsequent gas-solid reactions under highly dynamic conditions.

All the WL rim minerals are $^{16}$O-rich ($\Delta^{17}O = \sim -23‰$), indicating their formation in an $^{16}$O-rich nebular reservoir. Our Al-Mg measurements of hibonite, spinel, and diopside from the WL rim, as well as spinel and Al,Ti-diopside in the core, define a single, well-correlated isochron with an inferred initial $^{26}Al/^{27}Al$ ratio of $(4.94 \pm 0.12) \times 10^{-5}$. This indicates that the WL rim formed shortly after the host CAI. In contrast, the lack of $^{26}$Mg excesses in the WL rim anorthite suggest its later formation or later isotopic disturbance in the solar nebula, after $^{26}$Al had decayed.

*Keywords:* Wark-Lovering rim; Ca,Al-rich inclusion; solar nebula; microstructures; O isotopes; Al-Mg systematics.

## 1. INTRODUCTION

Wark-Lovering (WL) rims are thin (<100 μm) multi-layered mineral sequences that surround many Ca,Al-rich inclusions (CAIs). The rim layers consist of primary high-temperature minerals found in the CAI interiors, such as hibonite, perovskite, spinel, melilite, anorthite, Al,Ti-diopside, and/or forsterite. Wark and Boynton (2001) defined "classic" WL rims that consist of spinel, melilite, and diopside layers, but WL rims show considerable variations in their mineralogy and complexity among CAIs both within and among different chondrite groups (e.g., Bodénan et al., 2014; Simon et al., 2016; Krot et al., 2017a). Proposed models for the origin of WL rims include condensation (e.g., Wark and Lovering, 1977; Simon et al., 2005), metasomatic reaction (e.g., Ruzicka, 1997; MacPherson et al., 1981), evaporation (e.g., Wark and Boynton, 2001), or combinations of these (e.g., Keller et al., 2013; Simon et al., 2016). It is generally agreed that WL rims formed during high-temperature event(s) in the solar nebula after the host CAI formation but prior to accretion onto the parent body. Yet, the details of how and when WL rims formed and under what nebular conditions are poorly constrained.

Previous microstructural and isotopic studies of WL rims on CAIs in carbonaceous chondrites, mainly CV3 chondrites, have revealed their complex formation history in the early solar nebula. For example, transmission electron microscope (TEM) studies reported that many

WL rim layers consist of compact aggregates of micrometer-sized grains with partially-developed equilibrium grain boundary structures (Toppani et al., 2006; Zega et al., 2007, 2009, 2010; Keller et al., 2013), suggesting that WL rims formed largely by condensation, but melting could also be involved. Keller et al. (2013) reported an outermost forsterite layer consisting of columnar olivine grains with a common growth direction in a CAI from the Vigarano CV3 chondrite, consistent with growth from a vapor phase (Han et al., 2019). Based on electron backscattered diffraction (EBSD) analyses of CAIs in the Allende and Axtell CV3 chondrites, Bolser et al. (2016) showed that pyroxene grains have similar crystallographic orientations to each other and there is an epitaxial relationship between pyroxene and anorthite grains. These microstructures were interpreted to have resulted from high-temperature condensation from a nebular gas and subsequent oriented growth onto pre-existing layers. Stable Mg isotope measurements by Simon et al. (2005) showed that, unlike the elevated Mg isotopic compositions of the interiors of CV CAIs, their WL rims have systemically lower Mg isotope compositions ($\delta^{25}Mg \leq 0‰$, based on CI chondrites = 0.0‰ on the DSM3 scale), implying their formation at relatively high partial pressures of Mg in support of the view that WL rims represent the products of high-temperature condensation.

Magnesium isotopic studies of WL rims have given inconsistent views of the relative timing of the host CAI and WL rim formation events. Simon et al. (2005) concluded that WL rims formed soon after their host CAIs since their initial ($^{26}Al/^{27}Al$) ratios, $(^{26}Al/^{27}Al)_0$, were unresolvable. In contrast, Cosarinsky et al. (2007) and Matzel et al. (2015) reported differences between $(^{26}Al/^{27}Al)_0$ of CAI interiors and their WL rims in CM and CV chondrites, and concluded that WL rim may have formed up to 1 Ma after their host CAIs. Cosarinsky et al. (2007) also argued that WL rim formation occurred repeatedly during CAI formation, based on a comparison of $(^{26}Al/^{27}Al)_0$ in CV CAIs and their WL rims.

In addition, O isotopic studies of WL rims have revealed additional complexities in CAI dynamical histories. Complex O isotopic zoning patterns have been observed across WL rims on a number of CAIs from both oxidized and reduced CV3 chondrites, and melilite, anorthite, and Al,Ti-diopside are often $^{16}O$-depleted to various extents relative to hibonite and spinel (Cosarinsky et al., 2005; Taylor et al., 2005; Yoshitake et al., 2005; Ito et al., 2010; Simon et al., 2011, 2016). The isotopic heterogeneity among and within individual WL rim layers has been interpreted as evidence of nebular processing of CAIs in gaseous reservoirs having different O

isotopic compositions (Ito et al., 2010; Simon et al., 2011, 2016). In contrast, uniformly $^{16}$O-rich WL rims around CAIs are common in CM, CR, CH, and CO3.0 chondrites, which suggests that CAI evolution occurred within $^{16}$O-rich gas reservoir(s) (Matzel et al., 2013; Bodénan et al., 2014; Jacobsen et al., 2014; Krot et al., 2017a; Ushikubo et al., 2017). However, interpretations of O and Mg isotopic records in CV CAIs are complicated by possible overprints of fluid-rock interactions during thermal metamorphism on their parent asteroid (Bodénan et al., 2014; Krot et al., 2017a, b; 2019).

Coordinated microanalyses of WL rims are needed to best understand their origins and to decipher processes that they experienced in the nebula and parent body settings. Here we present the results of a comprehensive study of the mineralogy, petrology, microstructures, O isotopic compositions, and Al-Mg systematics of a WL rim on a Type B CAI, "*Big Guy*", from the reduced CV3 chondrite Vigarano. This inclusion is suited to this study because it displays a well-developed multi-layered sequence with little evidence for secondary parent body alteration. Our specific goals are: (1) to better describe the nature of the interfaces between the host CAI and the WL rim and between the WL rim layers, (2) to investigate textural and microstructural relationships between anorthite and associated phases, (3) to search for detectable variations in O and Mg isotopic composition across the WL rim layers, (4) to determine whether the WL rim formed contemporaneously with the host CAI, and (5) to provide better constraints on the contribution of each of high-temperature processes (e.g., condensation, melting, or evaporation) for the formation of the WL rim layers. We have a companion study that focuses on the *Big Guy* interior to investigate its O and Mg isotopic compositions, which will be discussed in detail elsewhere.

## 2. METHODS

### 2.1. Mineralogy and Petrology

The CAI *Big Guy*, in a thin section of Vigarano (USMNH 447), was studied by backscattered electron (BSE) imaging and X-ray elemental mapping using the JSC JEOL 7600F scanning electron microscope (SEM) equipped with a Thermo-Fisher silicon drift detector. Quantitative wavelength-dispersive spectroscopy analyses were obtained at JSC using both Cameca SX-100 and JEOL JXA-8530F electron probe microanalyzers (EPMAs). These measurements were performed at 15 kV accelerating voltage, 20 nA beam current, and 1 μm spot

size. Elemental calibration was carried out using synthetic and natural minerals, and data were reduced using the modified ZAF correction procedure PAP (Pouchou and Pichoir, 1984).

Six sections were prepared from the WL rim by the focused ion beam (FIB) technique using the JSC FEI Quanta 3D 600 dual beam FIB-SEM. Targeted regions for the sections covered all different mineral phases observed in the WL rim, including melilite in the mantle edge (Fig. EA1). The FIB sections were characterized in detail using bright-field (BF) and dark-field (DF) images, high-resolution (HR) images, and selected area electron diffraction (SAED), using the JSC JEOL 2500SE 200 kV field-emission scanning TEM (STEM). In addition, elemental mapping and quantitative microanalyses were carried out using a Thermo-Noran thin-window energy dispersive X-ray (EDX) spectrometer. Elemental X-ray maps were obtained using STEM raster mode with a scanned probe size of 2 nm and a dwell time of 50 μs/pixel. Successive rasters were added until <1% counting statistical errors were achieved for major elements. Data reduction was performed using the Cliff-Lorimer thin film approximation with experimental and theoretical K-factors determined from natural and synthetic standards.

### 2.2. Oxygen Isotopic Measurements

Oxygen isotopic measurements were conducted in transects across various locations of the *Big Guy* WL rim using the JSC CAMECA NanoSIMS 50L ion microprobe (Fig. EA2). A 16-18 pA $Cs^+$ primary beam, with a spot size of ~100 nm, was rastered over 7 × 7 μm areas to pre-sputter regions of interest, and O isotopic measurements were then performed on 5 × 5 μm or 3 × 3 μm areas within the pre-sputtered regions. $^{16}O^-$ was measured with a Faraday cup (FC) and $^{17}O^-$, $^{18}O^-$, $Si^-$, $MgO^-$, $AlO^-$, and $CaO^-$ were measured with electron multipliers (EMs) in multicollection. Measurements typically consisted of 20 cycles acquired over periods of 14 minutes. Terrestrial spinel, hibonite, and diopside standards were used to establish matrix corrections relative to olivine. San Carlos olivine standards were analyzed in the same analytical sessions using the same analytical procedures to correct for instrumental mass fractionation (IMF). The aging of EMs was monitored daily by obtaining pulse height distributions and the high voltage and/or deflection voltage were adjusted on each detector as necessary. Corrections for the EM dead time and quasi-simultaneous arrival were applied (Slodzian et al., 2004). An electron flood gun was used for charge compensation. A mass resolving power of >10,000 (Cameca definition) was achieved, sufficient to limit the contribution of $^{16}OH^-$ to $^{17}O^-$ to <0.1‰.

Data are reported as deviations from Standard Mean Ocean Water (SMOW), where $\delta^{17,18}O$ (‰) = $[((^{17,18}O/^{16}O)_{sample}/(^{17,18}O/^{16}O)_{SMOW}) - 1] \times 1000$, and as deviations from the terrestrial fractionation line, where $\Delta^{17}O$ (‰) = $\delta^{17}O - 0.52 \times \delta^{18}O$. For each analysis location that was analyzed once, errors are reported as two standard deviations of the mean of 20 cycles in the spot mode. For sample locations analyzed more than once, errors are reported as two standard deviations of the mean of multiple analyses (all image planes combined for each analysis).

### 2.3. Magnesium Isotopic Measurements

*In situ* isotope analyses of $^{26}Al$-$^{26}Mg$ were performed on the CAMECA ims-1290 ion microprobe at UCLA by slightly modifying a method described previously in Liu et al. (2018). Two analyses modes were used in the session. First, Mg-rich phases, such as hibonite, spinel, and diopside, were sputtered with a 1-1.5 nA $^{16}O_2^-$ primary ion beam ($\phi$ <4 μm) generated by a Hyperion-II oxygen plasma source, yielding Mg and Al secondary ion signals intense enough to be simultaneously measured with multiple FCs without switching the magnetic field setting. Each spot analysis consisted of 45 seconds of "pre-sputtering" and 300 seconds (10 seconds per cycle for 30 cycles) of data acquisition. Mass resolution (M/ΔM) was set at 2,500 (corresponding to exit slit #1 on the multicollection trolleys) to separate doubly-charged interferences ($^{48}Ca^{2+}$ and $^{48}Ti^{2+}$) from $^{24}Mg^+$. $^{24}MgH^+$ cannot be fully resolved from $^{25}Mg^+$ under such mass resolution, but the vacuum condition in the analysis chamber (pressure $\leq 1\times10^{-9}$ torr) made the hydride contribution negligible (<0.05‰). Second, peak-jumping monocollection was applied to analyze anorthite and gehlenitic melilite due to their low magnesium contents. The two phases were bombarded by a 70 pA primary ion beam and the secondary ions were collected with the axial EM. All ims-1290 ion microprobe spots are shown in Figure EA2.

Burma spinel, San Carlos olivine, San Carlos pyroxene, Madagascar hibonite, Miyakejima anorthite, and isotopically normal synthetic glasses of fassaite composition (known as "P0") and of melilite composition were used as standards to characterize IMF of Mg isotopes during ion probe analyses. The IMF is defined as

$$\alpha_i = \frac{\left(^{i}Mg/^{24}Mg\right)_m}{\left(^{i}Mg/^{24}Mg\right)_{true}}$$

, where i = 25 or 26, and m stands for "measured". All these terrestrial standards were assumed to have the "true" magnesium isotopic compositions of $^{25}Mg/^{24}Mg = 0.12663$ and $^{26}Mg/^{24}Mg =$

0.13932 (Catanzaro et al., 1966). $\alpha_{25}$ and $\alpha_{26}$ would have the following relationship when using an exponential mass fractionation law:

$$\alpha_{25} = (\alpha_{26})^{\beta}$$

$\beta$ is the IMF factor. This quantity was derived by first expressing the deviations of measured isotopic ratios from the assumed true values in modified delta-notation as:

$$\delta^{i}\mathrm{Mg}'\ (‰) = \ln \alpha_i \times 1000$$

, and then obtaining the slope of linear regression through data points on Mg-rich standards (Burma spinel, San Carlos olivine, and San Carlos pyroxene) in $\delta^{25}$Mg'-$\delta^{26}$Mg' space. The $\beta$ value was found to be 0.509, and is comparable to those obtained on other ims-1200 series ion microprobe (e.g., Villeneuve et al., 2009). The intrinsic mass-dependent fractionation of individual phases, expressed as $\delta^{25}$Mg, was calculated after correcting for the IMF by using $\alpha_{25}$ of the corresponding standard . The horizontal deviation from a mass fractionation line as a result of the decay of $^{26}$Al ($\equiv\Delta^{26}$Mg*) was calculated with the formula recommended in Davis et al. (2015):

$$\Delta^{26}\mathrm{Mg}^{*} = \delta^{26}\mathrm{Mg} - \left[\left(1 + \delta^{25}\mathrm{Mg}/1000\right)^{1/\beta} - 1\right] \times 1000$$

, where $\delta^{25,26}\mathrm{Mg} = (\alpha_{25,26} - 1) \times 1000$. In this study, $\delta^{i}$Mg and $\delta^{i}$Mg' are almost identical within errors. It should be pointed out that the calculated $\Delta^{26}$Mg* values depended very little on $\beta$ since the sample is not mass-fractionated significantly. The spots that would be most affected by the choice of $\beta$ are melilite spots with $\Delta^{26}$Mg* >15‰ because they are the most mass fractionated; however, the difference derived from choosing between $\beta$ = 0.509 and $\beta$ = 0.5128 (recommended by Davis et al., 2015) is no more than 0.2‰, which is totally within the quoted errors. The final reported error was calculated as:

$$\sigma_{\mathrm{final}} = \sqrt{\sigma^2_{\mathrm{internal}} + \sigma^2_{\mathrm{external}}}$$

, where $\sigma_{\mathrm{internal}}$ is the standard error of the mean $\Delta^{26}$Mg* on a cycle-by-cycle basis, and $\sigma_{\mathrm{external}}$ is the standard error of the mean of repeated measurements on the corresponding standard.
The relative sensitivity factor (RSF) of Al to Mg, defined as $(^{27}\mathrm{Al}/^{24}\mathrm{Mg})_{\mathrm{true}}/(^{27}\mathrm{Al}/^{24}\mathrm{Mg})_{\mathrm{m}}$, was characterized for different mineral phases by using the corresponding standards with known $^{27}$Al/$^{24}$Mg ratios. The true $^{27}$Al/$^{24}$Mg ratios of measured CAI minerals, including diopside, spinel, hibonite, melilite, and anorthite, were derived by applying the RSFs determined on P0 glass, Burma spinel, Madagascar hibonite, a synthetic melilite glass, and Miyakejima anorthite,

respectively. The RSF values and corresponding errors obtained in the session on each standard are listed in Table EA1.

## 3. RESULTS

The Vigarano CAI *Big Guy* is a 1,200 × 750 μm fragment of a coarse-grained Type B CAI (Fig. 1a). The CAI has a core-mantle-rim structure. The core, ~650 μm across, consists of blocky Al,Ti-rich diopside grains that poikilitically enclose euhedral spinel crystals. The ~200-600 μm wide mantle consists of zoned melilite grains that contain poikilitic euhedral spinel crystals. The mantle is surrounded by a ~30-100 μm thick WL rim which is overlain by a ~20-200 μm thick olivine-rich accretionary rim (Figs. 1b-c). We identified seven distinct layers in the WL rim sequence on *Big Guy*: (1) gehlenite in the outermost edge of the mantle, (2) hibonite, (3) spinel with lath-shaped hibonite and perovskite, (4) gehlenitic melilite, (5) anorthite, (6) zoned diopside grading outwards from Al,Ti-rich to Al,Ti-poor, and finally (7) forsteritic olivine intergrown with diopside. The accretionary rim consists of forsteritic olivine with minor metal and micro-CAIs. Alteration in this inclusion is relatively minor, similar to other inclusions from reduced CV chondrites, but in contrast to those in oxidized CV chondrites (Brearley and Krot, 2013).

### 3.1. Mineralogy and Petrology

Our TEM study shows that individual layers in the WL rim share several common features: (1) each layer consists of compact aggregates of micrometer to sub-micrometer sized crystals; (2) the interfaces between layers are highly convoluted and embayed; (3) curved grain boundaries between minerals are frequently observed; (4) crystallographic orientation relationships between adjacent minerals are uncommon, with most grains showing random orientations towards each another; and (5) most minerals are defect free. Below we describe in detail our TEM observations from the WL rim minerals, including mineral chemistry obtained using EPMAs (Table 1), and their O and Mg isotopic compositions.

#### 3.1.1. Gehlenite in the Mantle Edge

The CAI mantle is dominated by coarse melilite laths, ~250-450 μm in size, most of which are oriented at high angles to the rim, with heterogeneously distributed minor spinel

inclusions. In contrast, the outermost edge of the mantle consists of a 10-20 μm wide zone of micrometer-sized melilite grains with fine-grained inclusions of hibonite, perovskite, spinel, and grossite (Fig. 2). These melilite grains share a common growth orientation along (001) and contain abundant (001) planar defects (Fig. 2a). A rounded inclusion of grossite (pure and stoichiometric $CaAl_4O_7$; Table 2), ~2 μm in diameter, is completely surrounded by melilite with no contact with other oxide inclusions, at least within a two dimensional FIB section (Fig. 2b).

Electron microprobe traverse analyses of the mantle melilite show that their åkermanite content decreases gradually from $Åk_{\sim 60}$ at the core-mantle boundary to $Åk_{\sim 10\text{-}15}$ over a distance of ~30-100 μm from the core, then becomes relatively constant at $Åk_{\sim 10\text{-}15}$ through the rest of the mantle, and finally decreases gradually to $Åk_{\sim 0\text{-}5}$ over the outermost ~10-20 μm edge of the mantle (Fig. 2c). TEM EDX analysis reveals that melilite in contact with hibonite is uniformly end member gehlenite in composition (Table 2).

### 3.1.2. Hibonite

The CAI mantle is partially surrounded by a hibonite layer that varies from 3 to 30 μm (Figs. 1b-c). Hibonite crystals show a typical lath-shaped habit with a maximum length of ~12 μm and, unlike other WL rim minerals, usually share straight or slightly curved grain boundaries with each other (Fig. 3) and with gehlenite in the mantle edge (Fig. 2a). An analysis of electron diffraction patterns reveals that individual hibonite grains are consistently elongated normal to the *c* axis, but are randomly oriented relative to one another. We observed a single hibonite crystal in direct contact with melilite that contains a very low density of stacking defects, but most hibonite grains are free of stacking defects. Electron microprobe measurements show that hibonite contains 2.2-5.3 wt% $TiO_2$ and 1.4-2.8 wt% MgO (Table 1). Our TEM EDX analysis reveals no Mg zoning in hibonite grains.

Rounded gehlenite inclusions ≤2.5 μm in size are present in the innermost part of the hibonite layer (Fig. 3). A faceted refractory metal nugget (RMN) grain 120 nm in size is also included within hibonite as a homogeneous alloy enriched in Os, Ir, Ru, and Pt (in wt%: 40 Pt, 25 Ru, 13 Ir, 9 Os, 5 Mo, 4 W, 2 Fe, 1 Re, 1 Ni).

### 3.1.3. Spinel

A 5-35 μm wide spinel layer surrounds the hibonite layer, and its interface with hibonite

is highly embayed and curved (Fig. 4a). Elongated spinel rarely occurs in direct contact with the mantle melilite (Fig. 4b). Our EPMA analyses show that these spinel grains are essentially stoichiometric $MgAl_2O_4$ with 0.19-0.26 wt% $Cr_2O_3$ and 0.25-1.1 wt% FeO (Table 1), similar to that in the CAI interior. However, their $V_2O_3$ concentrations are lower in the WL rim (0.1-0.2 wt% $V_2O_3$) than in the CAI interior (0.3-0.6 wt% $V_2O_3$).

Numerous lath-shaped hibonite grains are included in spinel and these often surround partially to completely perovskite and/or elongated spinel grains (Figs. 1b-c, 4a-d). The hibonite inclusions contain stacking defects (Fig. 4c). Electron diffraction patterns obtained from these defect-structured hibonite grains show streaking along the *c* axis, and their lattice fringe images show irregular intergrowths of 2.6 nm (001) spacing within the dominant 2.2 nm (001) spacing of stoichiometric hibonite (Fig. 4e). Perovskite occurs commonly as inclusions in the spinel layer with equant to wormy morphologies (Figs. 1b-c, 4a-b). STEM imaging obtained from a single perovskite crystal shows the presence of multiple twin boundaries in the crystal (Fig. 4d), and its electron diffraction patterns are indexed as an intergrowth of [001] and [100] zones, consistent with twinning on (101) (Fig. 4f). In one instance, a crystallographic orientation relationship between spinel and perovskite is observed, such that $[130]_{spinel}//[120]_{perovskite}$ and $(001)_{spinel}//(001)_{perovskite}$ (Figs. 4g-h).

### 3.1.4. Melilite

A melilite layer is typically <10 μm wide, and straight grain boundaries with triple junctions are partially developed between melilite grains <5 μm in size (Figs. 5a-d). EPMA analyses of melilite contain 1.3-1.4 wt% MgO ($Åk_{\sim 9}$) (Table 1), but TEM EDX analysis reveals that individual melilite grains are zoned. In general, melilite is pure gehlenite ($Åk_{\sim 0}$) at the interface with spinel, but increases progressively in its åkermanite content up to $Åk_{\sim 10}$ towards the interfaces with anorthite and pyroxene (Fig. 5e). However, melilite in contact with pyroxene has higher åkermanite contents by ~3-4 mol% than that in contact with anorthite (Table 2). In addition, melilite contains no detectable Na even though it is spatially closely associated with local Na,Fe-rich amorphous materials of likely secondary parent body alteration origin.

Rounded spinel grains <1 μm in size rarely occur in the innermost part of the melilite layer. A faceted RMN 60 nm in size is included in melilite and is a homogeneous alloy enriched in Os, Ir, Ru, and Fe (in wt%: 42 Fe, 19 Ir, 15 Os, 7 Ru, 5 Mo, 5 Pt, 4 Ni, 2 W, 1 Re).

### 3.1.5. Anorthite

A discontinuous anorthite layer is developed between the melilite and pyroxene layers (Figs. 5b, d). This layer is 0.5-10 μm wide, but in most cases is less than 3 μm wide. Anorthite is in direct contact with spinel at the widest parts of the anorthite layer. Anorthite grains are typically <5 μm in size and show polysynthetic twinning. Minor spinel grains <1.5 μm in size occur as inclusions mostly in the inner part of the anorthite layer. Anorthite lacks crystallographic orientation relationships with adjacent melilite, spinel, and pyroxene. No accurate EPMA measurements of anorthite could be obtained because the anorthite layer is narrow and contains fine-grained spinel inclusions. However, TEM EDX analysis shows anorthite has a uniform composition of pure $CaAl_2Si_2O_8$ and contains no detectable Na (Table 2).

### 3.1.6. Diopside and Forsterite

Based on SEM BSE imaging and X-ray mapping, the outermost layer of the WL rim is a 3-40 μm wide layer of zoned diopside grading outwards from Al,Ti-rich to Al,Ti-poor (Figs. 1b-c). Rarely, Al,Ti-rich diopside occurs locally between spinel and melilite (Figs. 4b, 5a, 5c), and, based on TEM EDX analysis, show an uniform composition with 14 wt% $TiO_2$ and 29 wt% $Al_2O_3$ (Table 2). In addition, our TEM observations show that rare intergrowths of diopside and forsteritic olivine ($Fa_{\sim 3}$; Table 2) with convoluted interfaces (i.e., symplectic texture) are present in the outermost pyroxene layer (Fig. 6), and both diopside and forsterite share sharp contacts with porous aggregates of olivine grains in the accretionary rim. The diopside and forsterite grains range in size from 0.5 μm to 6 μm, and no crystallographic orientation relationships are observed between them. In general, diopside grains do not show any orientation relationships with each other, but rare clusters of some grains share a similar crystallographic orientation. In addition, subrounded spinel grains <1 μm in size occur as inclusions in the innermost diopside layer in direct contact with melilite (Figs. 5a, c).

Electron microprobe analyses show a compositional zoning in pyroxene, outward from Al,Ti-rich diopside to nearly endmember diopside (Table 1). Our TEM EDX analyses reveal an additional complexity in the pyroxene zoning. For example, Figures 5f and 5g show the variation in Al and Ti concentrations for the diopside layer along two different traverses: one where pyroxene is in contact with melilite and the other where it is in contact with anorthite. At the

anorthite-pyroxene interface, the Al and Ti contents decrease smoothly to their lowest values (Fig. 5g). In contrast, the situation is more complicated for pyroxene adjacent to melilite, where its Al and Ti contents decrease, then increase, and finally fall gradually to the lowest values (Fig. 5f). In general, the decrease in Al and Ti contents and the corresponding increase in Mg and Si contents are apparent over a ~2 μm distance from the interfaces of pyroxene with melilite and anorthite where the highest Al and Ti contents are observed. However, pyroxene immediately adjacent to anorthite contains lower Al contents and slightly higher Mg contents compared to that adjacent to melilite (Table 2).

### 3.2. Oxygen Isotopic Compositions

Oxygen isotopic compositions of individual minerals in the CAI *Big Guy*, obtained using NanoSIMS, are plotted in Figure 7 and listed in Table 3. On the $\delta^{17}O$ vs. $\delta^{18}O$ plot (Fig. 7a), oxygen isotopic compositions of all minerals from the CAI interior and the WL rim plot close to the carbonaceous chondrite anhydrous mineral line. Although all of the WL rim minerals are relatively $^{16}O$-rich, hibonite and spinel have lower $\delta^{17}O$ and $\delta^{18}O$ values relative to melilite, anorthite, and diopside. On the $\Delta^{17}O$ plot (Fig. 7b), all of the WL rim minerals have $^{16}O$-rich compositions with an average $\Delta^{17}O$ value of $-22.7 \pm 4.5$‰ ($\Delta^{17}O$ values ranging from −26‰ to −20‰). There are no resolvable variations in $\Delta^{17}O$ values across the entire WL rim sequence. In contrast to spinel both from the CAI core and mantle being $^{16}O$-rich ($\Delta^{17}O < -20$‰), the mantle melilite preserves a large variation in O isotopic compositions, with the most $^{16}O$-rich composition at the center of the mantle ($\Delta^{17}O = \sim -22$‰) and extending to $^{16}O$-poor maxima near the core-mantle and mantle-rim boundaries ($\Delta^{17}O = \sim 1$‰ and $\sim -2$‰, respectively).

### 3.3. Magnesium Isotopic Compositions

Magnesium isotopic compositions of individual minerals in the CAI *Big Guy* obtained using the ims-1290 ion microprobe are plotted on an $^{26}Al$-$^{26}Mg$ isochron diagram in Figure 8 and listed in Table 4. The high-precision multicollection data of hibonite, spinel, and diopside from the WL rim, as well as spinel and Al,Ti-rich diopside from the CAI interior, define a single well-correlated isochron, which yields a slope corresponding to $(^{26}Al/^{27}Al)_0 = (4.94 \pm 0.12) \times 10^{-5}$ ($\chi^2 = 1.8$) and an intercept of $0.09 \pm 0.04$‰ as the initial $\Delta^{26}Mg_0$* (errors are 2σ; Fig. 8a). The monocollection data of the mantle melilite are not regressed to infer its initial $^{26}Al/^{27}Al$ ratio

because of their large errors. However, the mantle melilite data are broadly consistent with the high precision data having $(^{26}Al/^{27}Al)_0 = 4.9 \times 10^{-5}$ at the 2σ level (Fig. 8b), except for a few of low $^{27}Al/^{24}Mg$ (<6) spots that are plotted below the regression line.

The WL rim anorthite appears to lack resolvable $^{26}Mg$ excesses (Table 4). The $^{27}Al/^{24}Mg$ ratios of anorthite range from ~10 to ~58 (Table 4), much lower than those that anorthite would usually have (e.g., 170-370; Kita et al., 2012). Our EPMA measurements of anorthite contained a significant amount of MgO (2.3-3.5 wt%), not listed in Table 1, due to the presence of fine spinel inclusions in anorthite, as confirmed by TEM analysis (Figs. 5b, d). The atomic ratios of Al/Mg range approximately from 9 to 12, which are in good agreement with $^{27}Al/^{24}Mg$ measured by the ims-1290 ion microprobe.

Variations in mass-dependent Mg isotopic fractionation (i.e., $\delta^{25}Mg$) are observed in the CAI interior and the WL rim (Table 4). The CAI interior minerals show isotopically heavy $\delta^{25}Mg$ = ~4-19‰, whereas the WL rim have relatively lower $\delta^{25}Mg$ values of ~−3-7‰. The distinct magnitudes of these variations observed in the CAI interior and the WL rim suggest that they were not derived from a single thermal event. In the CAI interior, spinel and Al,Ti-rich diopside are characterized by a constant $\delta^{25}Mg$ value of ~9‰. The mantle melilite has a range of $\delta^{25}Mg$ = ~4-19‰. However, melilite in direct contact with the WL rim has $\delta^{25}Mg$ = ~4-5‰, and hibonite grains completely surrounded by melilite in the mantle edge have $\delta^{25}Mg$ = ~7‰. In the WL rim, hibonite has mostly $\delta^{25}Mg$ <0‰, but one analysis shows a slightly increased $\delta^{25}Mg$ = ~3‰. All analyses of the WL rim spinel show consistent $\delta^{25}Mg$ <0‰. The $\delta^{25}Mg$ values of the WL rim diopside span from ~0‰ to ~2‰, whereas those of the WL rim anorthite have ~5-7‰.

## 4. DISCUSSION

### 4.1. High-Temperature Nebular History of the WL Rim

All the WL rim minerals in *Big Guy* are $^{16}O$-rich with $\Delta^{17}O$ = ~−23‰ (Fig. 7b; Table 3), indicating their formation in an $^{16}O$-rich gas reservoir. Importantly, melilite and anorthite retain $^{16}O$-rich compositions identical to those of other WL rim phases. However, we observed slightly elevated $\delta^{17}O$ and $\delta^{18}O$ values of melilite, anorthite, and diopside with respect to hibonite and spinel in the WL rim (Fig. 7a; Table 3). Here we consider whether these isotopic signatures represent the compositions of the WL rim minerals established in the solar nebula or modified by secondary parent body processes.

The $\Delta^{17}O$ value of ~−23‰ obtained from the *Big Guy* WL rim is characteristic of pristine or least metamorphosed CAI WL rims in CM, CO, CR, and most CH chondrites (Matzel et al., 2013; Bodénan et al., 2014; Jacobsen et al., 2014; Krot et al., 2017a, b; Ushikubo et al., 2017). This common composition is interpreted as a common source reservoir for many WL rims in the CAI-forming region. In contrast, most CAIs in metamorphosed CV chondrites including Vigarano show large variations in O isotopic compositions across their WL rims (Cosarinsky et al., 2005; Taylor et al., 2005; Yoshitake et al., 2005; Ito et al., 2010; Simon et al., 2011, 2016). Despite distinct, but complicated O isotopic records across WL rims in individual CV CAIs, the O isotopic heterogeneities in the WL rims are commonly associated with $^{16}O$-depleted melilite and anorthite ($\Delta^{17}O \geq \sim -10‰$). Some concerns have been raised that these isotopic records were disturbed by mineralogically controlled O isotope exchange with an $^{16}O$-poor fluid in the parent body setting (Wasson et al., 2001; Itoh et al., 2004; Krot et al., 2017b, 2019). However, the *Big Guy* WL rim does not show such significant O isotopic variations (Fig. 7b; Table 3), indicating that all the WL rim minerals preserve a primary nebular signature of $^{16}O$-rich reservoir during their formation and escaped a later-stage exchange with an $^{16}O$-poor reservoir both in the nebular and asteroidal settings.

Like many CV CAIs (Brearley and Krot, 2013), the WL rim minerals in *Big Guy* do contain petrological and compositional evidence for a relatively low, but limited degree of parent body metamorphic processes in the presence of fluid. This includes Fe enrichments along cracks and grain edges of spinel and olivine and the presence of Na,Fe-rich amorphous materials preferentially associated with melilite (Figs. 5a-d). However, other WL rim minerals, in particular melilite, are almost free of either Fe or Na enrichments, even at their grain boundaries, confirmed by TEM EDS (Table 2), despite their fine-grained nature. More importantly, we did not detect nepheline, sodalite, or grossular in the *Big Guy* WL rim that are common alteration products of melilite and anorthite found in other inclusions both from oxidized and reduced CV chondrite groups (Brearley and Krot, 2013). Additionally, two RMNs in hibonite and melilite show negative Mo anomalies of similar magnitude, compared to other refractory siderophiles relative to CI chondrites, and a less pronounced W depletion is also observed in the nugget in melilite (Fig. 9). These patterns are readily explained by high-temperature oxidation in the solar nebula, and limit the degree of low-temperature (<1,000 K) oxidation on the parent body, which causes larger W depletion or equal W and Mo depletions in RMNs (Fegley and Palme, 1985).

We therefore conclude that the *Big Guy* WL rim minerals experienced minimal modification in the parent body setting and remain largely unaltered. Thus, our coordinated analysis of the WL rim minerals presented here provide crucial constraints on high-temperature processing of primary refractory mineral assemblages in the solar nebula.

### 4.2. Formation Sequence of the WL Rim

The WL rim on *Big Guy* is a series of distinctive mineral layers that consist of refractory phases such as hibonite, perovskite, spinel, melilite, anorthite, diopside, and forsterite (Figs. 1b-c). The mineralogical and compositional characteristics of the WL rim minerals described above require a complex multi-stage high-temperature history including evaporation, melting, and gas-solid reactions, in which individual WL rim layers formed sequentially after the host CAI formation. We now explore in more detail a sequence for the formation of the WL rim layers, which is illustrated in Figure 10.

#### 4.2.1. Gehlenite and Hibonite: Flash Melting and Evaporation

Coarse melilite grains in the mantle radiate from the WL rim and are strongly zoned with åkermanite contents increasing away from the WL rim to the core (i.e., normal zoning) (Fig. 2c). These features are typically observed in Type B CAIs, and are evidence for inward growth of molten droplets that cooled by radiation of heat from their surfaces (e.g., MacPherson et al, 1984; Simon and Grossman, 2006). In contrast, at the outermost edge of the mantle, fine-grained, gehlenite grains occur beneath the hibonite layer (Fig. 2). The gehlenite grains share a common crystallographic orientation, contain a rare grossite inclusion, and are intimately intergrown with hibonite laths. The gehlenite grains are depleted in åkermanite content by at least ~10-15 mol% relative to the observed zoning trends of coarse melilite crystals in the mantle (Fig. 2c), as well as to initial melilite composition ($Åk_{>\sim 10\text{-}15}$) expected for a melt with *Big Guy* bulk composition, as predicted from phase relations of Stolper (1982). Anomalously gehlenitic melilite is observed at the edges of many coarse-grained CAIs just below the WL rim (e.g., Simon et al, 1999; Wark and Boynton, 2001; Yoshitake et al., 2005; Simon and Grossman, 2006; Simon et al., 2011; Bullock et al., 2013; Bolser et al., 2016;). Our TEM observations demonstrate for the first time that this compositional change is associated with textural changes over the narrow zone of the mantle edge. In addition, smaller but less variable $\delta^{25}$Mg values (~4-7‰) of gehlenite and

hibonite in the mantle edge are observed, compared to those (~9-19‰) of spinel and melilite in the CAI mantle (Table 4). Overall, the observed differences suggest that the outermost edge of the mantle represents a zone having higher Al/Mg than bulk composition of *Big Guy* that formed by high-temperature event(s) that occurred after the original *Big Guy* had crystallized.

The mantle edge may have been produced by high-temperature condensation of gehlenite and hibonite onto the original *Big Guy* mantle. In such a scenario, the decrease in åkermanite contents of melilite in the mantle edge towards the WL rim (Fig. 2c) would have resulted from a gradual drop of the total gas pressure during the condensation of melilite (MacPherson and Grossman, 1984). Condensation of hibonite onto gehlenite could have happened in the same nebular region where melilite condensed, but this would require the total gas pressure to drop by at least 2 orders of magnitude as the temperature remained constant above ~1,400K (Ebel, 2006). Alternatively, the original CAI may have been transported into a nebular region of higher temperature where hibonite and probably other WL rim minerals could resume condensation onto gehlenite. However, a condensation origin for gehlenite and hibonite in the mantle edge is difficult to reconcile with the common crystallographic orientation of gehlenite grains, straight grain boundaries between gehlenite and hibonite grains, and the perfectly rounded shape of grossite (Figs. 2-3).

Given the complications of the condensation origin, we conclude that it is more likely that gehlenite and hibonite formed by rapid crystallization from a thin, gehlenite-normative melt that was produced at the surface of the original *Big Guy* in a flash heating event. This hypothesis is supported by previous experimental studies showing the evolution of Mg, Si, Ca, and Al concentations with increasing a degree of evaporation (Hashimoto, 1983; Floss et al., 1996; Wang et al., 2001; Richter et al., 2002). In particular, Hashimoto (1991) showed that Mg evaporated at approximately twice the rate of Si, which evaporated ~8-9 times faster than Ca, without evaporative loss of Al, based on evaporation experiments of gehlenite and åkermanite.

Based on our measured zoning profile of melilite in the mantle (Fig. 2c), the original outermost mantle was likely composed of melilite with $Åk_{\sim 10\text{-}15}$. Even after short-lived melting of such melilite, Mg and Si would have evaporated nearly instantly, while Ca would have done so to a lesser degree and none of Al would be lost. The thin melt therefore became sufficiently Ca,Al-enriched to stabilize gehlenite, hibonite, and minor grossite. Previous equilibrium crystallization experiments showed that temperatures in excess of 1,500°C are required to

crystallize gehlenite from a Type B CAI-like melt (Mendybaev et al., 2006). In addition, Floss et al. (1996) produced hibonite only through evaporation at temperatures above 2,000°C and subsequent rapid cooling of bulk samples from the Allende CV3 chondrite. These results imply that, as an initial stage of the WL rim formation, gehlenite and hibonite crystallized rapidly from a Ca,Al-rich melt that formed on the surface of the original *Big Guy* by flash heating in excess of ~1,500°C and consequent evaporation of less refractory elements, Mg and Si, while the core and most of mantle remained largely unmodified. This high-temperature event should have happened after the mantle melilite had solidified and before a surrounding gas achieved a composition that formed subsequent layers from spinel to forsterite. However, gehlenite and hibonite in the mantle edge have relatively lower $\delta^{25}$Mg values compared to spinel and melilite in the CAI mantle (Table 4). The mantle edge may have become less fractionated by subsequent isotopic exchange with a nebular gas reservoir after rapid crystallization of gehlenite and hibonite, while the CAI mantle remained heavily mass fractionated due to an initial loss of Mg during the original CAI formation. We conclude that the layer of fine-grained gehlenite in the outermost edge of the mantle below the hibonite layer represents the initial base layer in the WL rim sequence.

Wark and Boyton (2001) invoked evaporation as an initial step in the WL rim formation, based on the parallel rare earth element patterns between the Type B1 CAI interiors and WL rims and the relative enrichments of highly refractory elements in the WL rims. They concluded that gehlenite and hibonite below the spinel layer were derived from refractory partial melts that formed at the outer mantle by evaporative loss of more volatile elements (Beckett and Stolper, 1994). This mechanism was favored by Simon et al. (1999) and Bullock et al. (2013) to explain the common presence of anomalously gehlenitic melilite at the margins of coarse-grained CAIs in CV3 chondrites. However, the relatively rare occurrence of hibonite in WL rims, different compositional ranges of melilite at the CAI margins, and variations in WL rim sequence suggest that different conditions (e.g., precursor bulk composition, melting temperatures, and cooling rates) in which evaporation took place are responsible for these variations observed from WL rims in individual CAIs.

In *Big Guy*, hibonite is the most refractory phase among the WL rim minerals (Figs. 1b-c) and no corundum is observed even at the nanometer scale, similar to other CAIs previously studied. Simon et al. (1994) proposed that the paucity of corundum-bearing inclusions was due to the instability of corundum relative to hibonite in the presence of small amounts of oxides other

than $Al_2O_3$ in melts. A partial melt produced at the *Big Guy* surface likely contained variable amounts of Ca, Mg, Ti, and Si, depending on the relative amounts of melilite, spinel, and perovskite melted and the degree of evaporation. Evaporative loss of Ca is required to stabilize corundum, but it can form only after almost complete loss of Mg and Si by extensive evaporation at very high temperatures above 2,000 K (Floss et al., 1998; Simon and DePaolo, 2010). Thus, most of CaO and possibly $TiO_2$ were preserved in the melt, and consequently corundum could not crystallize and instead hibonite crystallized. In addition, we observed the rare, rounded grossite inclusion in gehlenite below the hibonite layer (Fig. 2b), suggesting its crystallization from a melt during gehlenite crystallization. The rarity of grossite contrasts with the results of previous evaporation experiments that showed that grossite appeared as a stable stoichiometric phase in the residues with higher mass losses (Ireland and Esat, 1986; Mendybaev et al., 2006). However, the stability field of grossite appears to be greatly reduced by the presence of Mg and Ti in a melt, with a corresponding expansion of the stability field of spinel and hibonite, as experimentally demonstrated by Beckett and Stolper (1994) and Han et al. (2016). The survival of grossite in gehlenite may therefore be due to a melt of extremely gehlenite-normative composition (Beckett and Stolper, 1994; Weber and Bischoff, 1994).

Hibonite in the *Big Guy* WL rim contains significant Mg and Ti (Tables 1 and 2), similar to the ranges observed in other CAIs and WL rims (Brearley and Jones, 1998). Most of the WL rim hibonites are isotopically light ($\delta^{25}$Mg <0‰), whereas the CAI interior shows heavy Mg isotopic compositions ($\delta^{25}$Mg = ~4-19‰; Table 4). Several lines of evidence suggest that these compositions of the WL rim hibonite resulted from chemical and isotopic exchange with a nebular gas reservoir after the initial stages of WL rim formation. First, the gradual decrease of åkermanite contents in melilite and the presence of hibonite intergrown with gehlenite in the mantle edge (Fig. 2) imply a substantial loss of the original Mg during melting and evaporation. Second, elevated Mg and Ti contents in the WL rim hibonite are different from Mg-free hibonite with <1 wt% $TiO_2$ that formed by evaporation experiments (Ireland and Esat, 1986; Floss et al., 1996). Third, the *Big Guy* mantle lacks sufficient Ti-bearing phases that would be needed for growth of Ti-bearing hibonite from a melt. Considering the Ti partition coefficient between hibonite and melt (0.8-2.1; Beckett and Stolper, 1994), hibonite with ~2-5 wt% $TiO_2$ (Table 1) would require a melt with at least ~2 wt% $TiO_2$. We did not observe enough perovskite in the mantle to produce a melt with such high Ti contents. In addition, melting all perovskite present

would require extreme conditions of proloned exposure to very high temperatures (above ~2,000°C) in order to melt melilite that encloses perovskite. Moreover, a heating event intense enough to melt perovskite would lead to a significant evaporative loss of Ti from the melt (Floss et al., 1998; Wang et al., 2001). Finally, the Mg isotopic compositions of WL rim minerals (Table 4) are inconsistent with any significant Mg isotopic fractionation due to evaporative loss (e.g., Floss et al., 1996; Wang et al., 2001; Richter et al., 2002). We therefore conclude that the observed chemical and isotopic compositions of the WL rim hibonite was achieved by solid-state re-equilibration with the surrounding gas reservoir having a normal Mg isotopic composition during or before spinel formation (Simon et al., 2005; Young et al., 2005; Simon and Young, 2011).

This conclusion is further supported by systematically lower $\delta^{25}$Mg values (~4-7‰) of gehlenite and hibonite in the mantle edge, relative to melilite and spinel in the mantle ($\delta^{25}$Mg = ~9-19‰; Table 4), which requires later Mg isotopic exchange at the mantle edge with an external gas reservoir after the original CAI formation (Simon et al., 2005; Simon and Young, 2011; Kita et al., 2012; Bullock et al., 2013). Only one analysis of the WL rim hibonite adjacent to the mantle melilite shows elevated Mg isotopic fractionation with $\delta^{25}$Mg = ~3‰, but most are isotopically light with $\delta^{25}$Mg <0‰ (Table 4). This variation may reflect varying degrees of Mg isotopic exchange with an external isotopically normal gas reservoir.

### 4.2.2. Spinel, Melilite, Diopside, and Forsterite: Disequilibrium Gas-Solid Condensation

Detailed examinations of the WL rim layers from spinel to forsterite give further clues to the rim formation process. The outer layers of the WL rim consist of spinel, melilite ($Åk_{<\sim10}$), anorthite, diopside, and forsterite (Figs. 1b-c), which become less refractory outwards from the CAI mantle edge composed of gehlenite and hibonite. In particular, we observed the fine scale zoning observed in individual melilite and diopside grains (Table 2; Figs. 5e-g); melilite increases progressively in åkermanite content outwards, whereas diopside shows gradual decreases in Al and Ti contents. All minerals are fine grained (≤~5 μm), and share highly curved grain boundaries with each other (Figs. 4-6). These observations suggest that layers of spinel to forsterite condensed onto hibonite under highly dynamic conditions, probably at high partial pressures of gaseous SiO and Mg (Simon et al., 2005; Toppani et al., 2006; Keller et al., 2013).

Following the flash heating event that formed gehlenite and hibonite in the mantle edge,

spinel formed by reaction of hibonite with gaseous Mg, and minor fine-grained perovskite also formed by incorporating Ca and Ti of hibonite (Wark and Lovering, 1977). Evidence for such gas-solid reactions to replace hibonite by spinel and minor perovskite is based on (1) the embayed appearance of hibonite by spinel (Fig. 4a), (2) the presence of abundant hibonite and perovskite inclusions in spinel (Figs. 1b-c, 4b), (3) the occurrence of elongated spinel enclosed in some hibonite inclusions in spinel (Fig. 4c), (4) the crystallographic orientation relationship between perovskite and spinel (Figs. 4g-h), and (5) the rare platy morphology of spinel in direct contact with the mantle (Fig. 4b). Importantly, hibonite inclusions in spinel contain stacking defects, showing a variation in lattice spacing (Fig. 4e). Ideal hibonite consists of a sequence of one spinel block alternating with one Ca-containing block, resulting in a 2.2 nm wide unit cell parallel to (001) (Nagashima et al., 2010). In contrast, the local presence of 2.6 nm wide (001) layers in hibonite can be interpreted as complex intergrowths of stoichiometric and disordered, Mg-enriched hibonite as a result of the formation of thicker spinel blocks by substitution of Mg with Al in spinel blocks only (Schmid and De Jonghe, 1983; Han et al., 2015). Hibonite reacted with the nebular gas and had been partially replaced by spinel under disequilibrium conditions, where kinetic effects may play a significant role in stabilizing defect-structured hibonite and spinel rather than hibonite and corundum (Han et al., 2015). The reaction involving hibonite clearly did not go to completion so hibonite contains wider spinel blocks (i.e., stacking defects; Fig. 4e) and occurs as a discontinuous layer onto the mantle and as inclusions with perovskite in the spinel layer (Figs. 4a-d).

Melilite apparently formed after spinel in the *Big Guy* WL rim, opposite to equilibrium condensation calculations that predict melilite condensation before spinel (Ebel, 2006). As inferred from the crystallographic continuity of spinel with hibonite by Han et al. (2015), a structural similarity between hibonite and spinel (i.e., hexagonal arrangements of O ions in $(001)_{hibonite}$ and $(111)_{spinel}$) may have caused kinetic inhibition of melilite condensation and instead stabilized nucleation and growth of spinel onto pre-existing surfaces of hibonite (Beckett and Stolper, 1994). Although direct TEM observations of a crystallographic orientation relationship between hibonite and spinel were not made in this study, the late condensation of melilite after spinel could be also supported by the presence of stacking defects in hibonite enclosed in spinel (Fig. 4e), which represents the structural disturbance of hibonite due to the formation of wider spinel blocks. Melilite may have begun to condense onto spinel by reaction of

spinel ± hibonite with gaseous SiO, Mg, and possibly Ca, and became progressively more åkermanitic (Yoneda and Grossman, 1995).

Surrounding the melilite layer is a zoned diopside layer with minor spinel concentrated in the innermost layer (Figs. 5a, c). In contrast to other rim minerals, diopside shows large compositional variations in Al and Ti contents decreasing away from melilite over very short distances of <~2 μm (Fig. 5f), which has been widely recognized in many WL rims (e.g., Wark and Lovering, 1977; Simon et al., 2007; Ito et al., 2010; Zega et al., 2010; Keller et al., 2013). The highest $Al_2O_3$ and $TiO_2$ contents in diopside are observed at the interface with melilite along with the complete absence of Ti-rich reactant solid phases (i.e., perovskite) (Figs. 5a, c), suggesting that the earliest stages of diopside formation involved a reaction of melilite with gaseous Mg, SiO, and Ti to form Al,Ti-rich diopside and minor spinel (Han and Brearley, 2016; Krot et al., 2017a). As the reaction proceeded, the gas became depleted in Ti, and the condensing diopside composition evolved outwards from Al,Ti-rich at the interface with melilite to Al,Ti-poor that occurs on the outer part of the pyroxene layer. Rarely, uniformly Al,Ti-rich diopside grains occur between spinel and melilite (Figs. 4b, 5a, 5c), suggesting that both spinel and melilite were partially reacted to form Al,Ti-rich diopside under disequilibrium conditions.

Our TEM observations confirm that the discontinuous layers of forsterite intimately intergrown with diospide occurs below the diopside layer (Fig. 6), which were not readily identified based on the SEM techniques alone due to the well-developed accretionary rim on *Big Guy* (Fig. 1). The similar textural relationship between diopside and forsterite in the outermost WL rims was reported on other inclusions from the same meteorite by Ito et al. (2010) and Keller et al. (2013). We therefore conclude that the final stage of the WL rim formation involved the minor condensation of forsterite with diopside over a limited time after the bulk of the diopside layer had formed. The sharp grain boundaries between the WL rim and the accretionary rim and their different porosity nature suggest that most forsterite condensed as a separate event after the WL rim formation and accreted later onto the WL rim.

Based on combined EBSD and TEM study of the WL rims around melilite-rich CAIs from the Axtell and Allende CV3 chondrites, Bolser et al. (2016) observed numerous pyroxene and anorthite grains in similar crystallographic orientations as well as epitaxial relationship between some anorthite and pyroxene grains. In contrast, our analysis of electron diffraction patterns obtained from the WL rim minerals in all the FIB sections reveals that only a few

diopside grains are in a close orientation, and most minerals are randomly oriented to each other, consistent with previous TEM studies (e.g., Toppani et al., 2006; Keller et al., 2013). The inconsistency may have arisen because our FIB sections sampled only up to several tens of grains, in most cases fewer than 10 grains in each layer, in comparison with >1,000 pyroxene grains and >100 anorthite grains examined by Bolser et al. (2016). A few grains therefore may have condensed in a similar orientation, possibly in the form of three dimensional islands onto pre-existing grain surfaces as a result of surface free energy minimization during high-temperature condensation (Bolser et al., 2016). However, it is likely that the majority of the WL rim minerals had nucleated and grown in random orientations onto early-formed mineral surfaces.

### 4.2.3. Anorthite: Late Nebular Alteration of Melilite and Al-Diopside

Anorthite occurs as a discontinuous layer between melilite and Al,Ti-rich diopside, often with minor spinel (Figs. 5b, d). Melilite and diopside in contact with anorthite are corroded and embayed. Melilite and diopside show distinct composition ranges depending on the presence of anorthite between these two phases; at the grain boundaries where anorthite is present, melilite is less åkermanitic, whereas pyroxene has lower $Al_2O_3$, slightly higher MgO (Figs. 5f-g; Table 2). These observations imply that anorthite formed later by reaction with melilite and Al-diopside with gaseous SiO. Incorporation of gaseous Mg may have been necessary to form diopside and possibly minor spinel. A similar gas-solid reaction involving the replacement of melilite by fine-grained assemblages of anorthite, diopside, and ±spinel was inferred previously from WL rims in CR chondrites (Krot et al., 2017a) and AOAs in various carbonaceous chondrite groups (e.g., Han and Brearley, 2015; Ushikubo et al., 2017).

Anorthite lacks evidence for *in situ* decay of $^{26}Al$, consistent with formation at least 3 Ma after other WL rim minerals in the solar nebula. Matzel et al. (2015) inferred an age gap of up to 1 Ma between the host CAI and WL rim, based on NanoSIMS measurements from a uniformly $^{16}O$-rich ($\Delta^{17}O = \sim -24‰$) Type A CAI MUM-1 in the Murchison CM2 chondrite that exhibits $(^{26}Al/^{27}Al)_0 \approx 2.0 \times 10^{-5}$ for anorthite in the WL rim and $(^{26}Al/^{27}Al)_0 \approx 5.0 \times 10^{-5}$ for melilite and spinel in the interior. This potential age gap would require a later high-temperature event that introduced gaseous SiO and Mg to react with melilite and Al-diopside to form anorthite with minor diopside and spinel in the WL rim, possibly after formation of the WL rim forsterite layer.

Such an event may have led to condensation of the accretionary rim forsterite on the exterior of the WL rim. The $^{16}$O-rich composition of anorthite ($\Delta^{17}O$ = ~−22‰; Fig. 7; Table 3) indicates that it must have formed in the presence of an $^{16}$O-rich gas reservoir after the formation of other WL rim layers. A similar conclusion was inferred by Ushikubo et al. (2017) from a fine-grained CAI G92 in the Acfer 094 chondrite that is uniformly $^{16}$O-rich ($\Delta^{17}O$ = ~−23‰), but has anorthite with a distinctly lower $(^{26}Al/^{27}Al)_0 = 5.21 \times 10^{-6}$, compared to Al,Ti-rich diopside and melilite having $(^{26}Al/^{27}Al)_0 = 5.2 \times 10^{-5}$.

Alternatively, the lack of $^{26}$Mg excesses in the WL rim anorthite could have resulted from Mg isotopic resetting event(s) either in the solar nebula or in the parent body environment. Previous Al-Mg isotopic studies of many CAIs suggested that episodic heating events repeatedly occurred in the solar nebula (e.g., Kita et al., 2012; MacPherson et al., 2012; Kawasaki et al., 2019). Anorthite may have formed simultaneously with other WL rim minerals at $(^{26}Al/^{27}Al)_0 = 4.94 \times 10^{-5}$ (Fig. 8a) and later lost its radiogenic $^{26}$Mg excesses during thermal processing in the solar nebula. However, if this was the case, one would expect complementary phases with anomalously high $\Delta^{26}$Mg* values that plot well above the isochron (Podosek et al., 1991; MacPherson et al., 2012) or with a high $\Delta^{26}$Mg* intercept (Young et al., 2005; Simon and Young, 2011). Fine spinel inclusions in anorthite (Figs. 5b, d) could have increased their $\Delta^{26}$Mg* values by Mg isotopic exchange with anorthite that had originally $^{26}$Mg excesses. However, variations in $\Delta^{26}$Mg* at the scale less than a micrometer are impossible to resolve spatially using the ims-1290 ion microprobe. We therefore cannot completely rule out the possibility that thermal event(s) in the solar nebula caused a complete Mg isotopic exchange between anorthite and adjacent phases, such as spinel.

Radiogenic $^{26}$Mg excesses in the WL rim anorthite could have been lost due to Mg isotope diffusive exchange induced by thermal metamorphism on the parent body (LaTourrette and Wasserburg, 1998; Ito and Messenger, 2010). However, the $^{16}$O-rich compositions of the WL rim minerals, including anorthite (Fig. 7; Table 3), preclude thermal metamorphism, as discussed in section 4.1, and indicate the preservation of their original Mg isotopic compositions recorded in the solar nebula. Since O in anorthite diffuses faster than Mg by 2-3 orders of magnitude at 400-500°C (Ryerson and McKeegan, 1994; LaTourrette and Wasserburg, 1998), its original O isotope composition would be more effectively disturbed than its Mg isotopic composition even by mild thermal metamorphism, which is obviously not the case for *Big Guy*.

Thus, we conclude that the WL rim anorthite represents a nebular product whose Mg isotopic compositions reflect either delayed anorthite formation after $^{26}$Al had completely decayed or late-stage thermal event(s) in the solar nebula that erased completely any evidence for live $^{26}$Al in anorthite.

### 4.2.4. Nebular Conditions for the WL Rim Formation

Collectively, our observations are interpreted as evidence for two main events to form the WL rim after the host CAI *Big Guy* formation: rapid crystallization of gehlenite and hibonite after flash melting and extensive evaporation of the original CAI edge, followed by a series of gas-solid replacement reactions to produce spinel, melilite, diopside, forsterite, and finally anorthite. Implicit is that the formation processes and conditions of the WL rim were different from those of the CAI interior, as clearly indicated by differences in mineralogical and petrologic characteristics and chemical and isotopic compositions between the CAI interior and the WL rim. For example, the relative depletions of V contents of spinel in the WL rim compared to those in the CAI interior suggest that the WL rim formed under relatively more oxidizing conditions as V is even more volatile at higher O fugacities (Wark and Boyton, 2001). In addition, two RMNs in the WL rim show negative Mo anomalies with no or slight negative W anomalies (Fig. 9), which provide evidence that their chemistry was established at high-temperatures in a relatively oxidizing region of the solar nebula because Mo and W become more volatile at increased O fugacities (Fegley and Palme, 1985). As discussed by Simon et al. (2005), the low $\delta^{25}$Mg values of the WL rim minerals relative to the host CAI (Table 4) reflect an increase in the partial pressure of Mg (and apparently SiO) during the WL rim formation. Such nebular conditions (i.e., high temperatures and high gas pressures of Mg, SiO, and O) may have achieved by local transient heating and subsequent evaporation that was the very first step for the WL rim formation, as discussed in section 4.2.1, or by rapid transport into a region of the solar nebula that had been at different conditions than those during the host CAI formation as a consequence of the solar nebular evolution (Ciesla, 2010; Boss et al., 2012).

## 4.3. Timing of the WL Rim Formation

Hibonite, spinel, and diopside measured from *Big Guy* using the ims-1290 ion microprobe define a well-correlated isochron corresponding to $(^{26}Al/^{27}Al)_0 = 4.94 \times 10^{-5}$ (Fig.

8a). This ratio represents a timing when nebula-wide thermal processing took place (Liu et al., 2019). We conclude that there is no discernable age gap between the formation of the CAI interior and the WL rim; that is, *Big Guy* crystallized from a melt ~$5 \times 10^4$ years after the canonical value was established, and then high-temperature reprocessing that enabled the WL rim minerals to form occurred very rapidly soon after the CAI interior crystallized. A similar conclusion was inferred based on indistinguishable $(^{26}Al/^{27}Al)_0$ ranges of the interior and the WL rim phases from Type A and B CAIs in CV3 chondrites (Simon et al., 2005; Cosarinsky et al., 2007; Kawasaki et al., 2019). Differences in $(^{26}Al/^{27}Al)_0$ between CAIs and their WL rims were also reported from Type A CAIs in CV and CM chondrites (Cosarinsky et al., 2007; Matzel et al., 2015), suggesting significant age gaps between the CAI interior and the WL rim formation up to ~0.2 Ma. Collectively, the observed spread in $(^{26}Al/^{27}Al)_0$ of WL rims ranging from $4.4\times10^{-5}$ to $5.6\times10^{-5}$ (Simon et al., 2005; Cosarinsky et al., 2007; Kawasaki et al., 2019; this study) indicates that episodic high-temperature events leading to the WL rim formation (and apparently CAI reprocessing after initial formation by condensation) occurred repeatedly in the solar nebula for a prolonged period of time at least ~0.2 Ma (e.g., Cosarinsky et al., 2007; Kita et al., 2012; MacPherson et al., 2012; Ushikubo et al., 2017; Kawasaki et al., 2019).

## 5. CONCLUSIONS

Our study reveals seven layers in the WL rim from the Vigarano CAI *Big Guy* that include: (1) gehlenite in the outermost edge of the mantle, (2) hibonite, (3) spinel with hibonite and perovskite, (4) zoned melilite ($Åk_{\sim0\text{-}10}$), (5) anorthite, (6) zoned diopside grading outwards from Al,Ti-rich to Al,Ti-poor, and (7) forsterite intergrown with diopside just below the olivine-rich accretionary rim. We conclude that the WL rim formation was initiated by flash melting and extensive evaporation of the original CAI edge, followed by rapid crystallization and subsequent gas-solid reactions under highly dynamic conditions (Fig. 10). Here, the important observations obtained using TEM, NanoSIMS, and SIMS and their implication for the formation of the WL rim sequence on *Big Guy* were summarized, as follows:

(1) The mantle contains normally-zoned, coarse melilite grains, whereas the mantle edge consists of fine-grained gehlenite grains that share a common growth orientation with hibonite and rare grossite. These phases in the mantle edge likely crystallized rapidly from a thin Ca,Al-rich melt layer that formed at the original inclusion surface by flash

melting in excess of 1,500°C and preferential evaporation of less refractory elements, Mg and Si, after crystallization of the original inclusion.

(2) The CAI mantle edge composed of gehlenite and hibonite is surrounded by successive layers of spinel, melilite, diopside, and forsterite, suggesting sequential condensation of spinel, melilite, diopside, and forsterite. The lower $\delta^{25}$Mg compositions of the WL rim minerals compared to the CAI interior imply that the WL rim formed by condensation at increased pressures of Mg (and SiO).

(3) Anorthite occurs as a discontinuous layer that corrodes adjacent melilite and Al,Ti-rich diopside, often with spinel. At the interfaces with anorthite, melilite is less åkermanitic, and diopside contains lower Al, but slightly higher Mg contents. These observations can be interpreted as evidence for an additional, even later, reaction of melilite and Al-diopside with gaseous SiO and Mg to form anorthite with minor diopside and spinel, probably after forsterite condensation.

(4) All the WL rim minerals including melilite and anorthite are $^{16}$O-rich ($\Delta^{17}O$ = ~−23‰), indicating their formation in an $^{16}$O-rich gas reservoir. Our data are in contrast with many CV CAIs that show heterogeneous O isotopic compositions across their WL rims.

(5) Our Al-Mg data of the CAI interior and the WL rim define a well-correlated isochron with $(^{26}Al/^{27}Al)_0 = 4.94 \times 10^{-5}$, indicating their synchronous formation ~$5 \times 10^4$ years after the canonical value. In contrast, no $^{26}$Mg excesses is observed from the WL rim anorthite, which suggests its later formation or later isotopic resetting in the solar nebula, after $^{26}$Al had decayed.

**ACKNOWLEDGEMENTS**

We thank Dr. Ushikubo, Dr. Krot, and an anonymous reviewer for their helpful and constructive comments. Editorial handling by Dr. Krot is greatly appreciated. This study was supported in part by NASA grants 10-COS10-0049, 14-EW14_2-122, and 17-EW17_2-0148 (LPK); 80NSSC18K0602 (MCL); 13-COS13-0018 (SM); and 16-EW16_2-0163 (JIS). LPI contribution No. 2234. LPI is operated by USRA under a cooperative agreement with the Science Mission Directorate of the National Aeronautics and Space Administration. The UCLA ims-1290 ion microprobe facility is partially supported by a grant from the NSF Instrumentation

and Facilities program, for which the authors are grateful.

## REFERENCES


Beckett J. R. and Stolper E. (1994) The stability of hibonite, melilite, and other aluminous phases in silicate melts: Implications for the origin of hibonite-bearing inclusions from carbonaceous chondrites. Meteoritics 29, 41-65.

Bodénan J.-D., Starkey N. A., Russell S. S., Wright I. P. and Franchi I. A. (2014) An oxygen isotope study of Wark–Lovering rims on type A CAIs in primitive carbonaceous chondrites. Earth Planet. Sci. Lett. 401, 327-336.

Bolser D., Zega T. J., Asaduzzaman A., Bringuier S., Simon S. B., Grossman L., Thompson M. S. and Domanik K. J. (2016) Microstructural analysis of Wark-Lovering rims in the Allende and Axtell CV3 chondrites: Implications for high-temperature nebular processes. Meteorit. Planet. Sci. 51, 743–756.

Boss A. P., Alexander C. M. O'D. and Podolak M. (2012) Cosmochemical consequences of particle trajectories during FU Orionis outbursts by the early Sun. Earth Planet. Sci. Lett. 345–348, 18–26.

Brearley A. J. and Jones R. H. (1998) Chondritic meteorites. In: Reviews in Mineralogy, Volume 36. Planetary Materials. (Ed. J.J. Papike). pp. 3-001-3-398.

Brearley A. J. and Krot A. N. (2013) Metasomatism in the early solar system: the record from chondritic meteorites. In Metasomatism and the Chemical Transformation of Rock (eds. D. E. Harlov and A. Austrheim). Springer, Berlin Heidelberg, pp. 659–789.

Bullock E. S., Knight K. B., Richter F. M., Kita N. T., Ushikubo T., MacPherson G. J., Davis A. M. and Mendybaev R. A. (2013) Mg and Si isotopic fractionation patterns in types B1 and B2 CAIs: Implications for formation under different nebular conditions. Meteorit. Planet. Sci. 48, 1440–1458.

Catanazaro E. J., Murphy T. J., Garner E. L. and Shields W. R. (1966) Absolute isotopic abundance ratios and atomic weights of magnesium. J. Res. NBS 70A, 453–458.

Ciesla F. J. (2010) The distributions and ages of refractory objects in the solar nebula. Icarus 208, 455–467.

Cosarinsky M., McKeegan K. D., Hutcheon I. D., Weber P. and Fallon S. (2005) Magnesium and oxygen isotopic study of the Wark-Lovering rim around a fluffy Type A inclusion from Allende. 36th Lunar and Planetary Science conference. Abstract #2105.

Cosarinsky M., Taylor D. J., Liu M.-C, McKeegan K. D. and Krot A. N. (2007) Distribution of aluminum-26 in refractory inclusions from CV chondrites. Workshop on Chronology of Meteorites. Abstract #4052.

Davis A. M., Richter F. M., Mendybaev R. A., Janney P. E., Wadhwa M. and McKeegan K. D. (2015) Isotopic mass fractionation laws for magnesium and their effects on $^{26}$Al–$^{26}$Mg systematics in solar system materials. Geochim. Cosmochim. Acta 158, 245–261.

Ebel D. S. (2006) Condensation of rocky material in astrophysical environments. In Meteorites and the Early Solar System II (eds. D. S. Lauretta and , Jr.H. Y. McSween). University of Arizona Press, Tucson, pp. 253–277.

Fegley B. and Palme H. (1985) Evidence for oxidizing conditions in the solar nebula from Mo and W depletions in refractory inclusions in carbonaceous chondrites. Earth Planet. Sci. Lett. 72, 311-326.

Floss C., El Goresy A., Zinner E., Kransel G., Rammensee W. and Palme H. (1996) Elemental and isotopic fractionations produced through evaporation of the Allende CV chondrite: Implications for the origin of HAL-type hibonite inclusions. Geochim. Cosmochim. Acta

60, 1975-1997.
Floss C., El Goresy A., Zinner E., Palme H., Weckwerth G. and Rammensee W. (1998) Corundum-bearing residues produced through evaporation of natural and synthetic hibonite. Meteorit. Planet. Sci. 33, 191–206.
Han J. and Brearley A. J. (2016) Microstructural constraints on complex thermal histories of refractory CAI-like objects in an amoeboid olivine aggregate from the ALHA77307 CO3.0 chondrite. Geochim. Cosmochim. Acta 183, 176–197.
Han J., Brearley A. J. and Keller L. P. (2015) Microstructural evidence for a disequilibrium condensation origin for hibonite-spinel inclusions in the ALHA77307 CO3.0 chondrite. Meteorit. Planet. Sci. 50, 2121–2136.
Han J., Keller L. P., Brearley A. J. and Danielson L. R. (2016) Stacking defects in synthetic and meteoritic hibonites: implications for high-temperature processes in the solar nebula. 47th Lunar and Planetary Science Conference. Abstract #2848.
Han J., Jacobsen B., Liu M.-C., Brearley A. J., Matzel J. E. and Keller L. P. (2019) Origin of $^{16}$O-rich fine-grained Ca-Al-rich inclusions of different mineralogy and texture. *Geochemistry*, doi: https://doi.org/10.1016/j.chemer.2019.125543.
Hashimoto A. (1983) Evaporation metamorphism in the early solar nebula—Evaporation experiments on the melt FeO-MgO-$SiO_2$-CaO-$Al_2O_3$ and chemical fractionations of primitive materials. Geochem. J. 17, 111–145.
Hashimoto (1991) Evaporation of melilite. Meteoritics 26, 344.
Ito M. and Ganguly J. (2009) Magnesium diffusion in minerals in CAIs: New experimental data for melilites and implications for the Al-Mg chronometer and thermal history of CAIs. 40th Lunar and Planetary Science Conference. Abstract #1753.
Ito M. and Messenger S. (2010) Thermal metamorphic history of a Ca, Al-rich inclusion constrained by high spatial resolution Mg isotopic measurements with NanoSIMS 50L. Meteorit. Planet. Sci. 45, 583–595.
Ito M., Messenger S., Keller L. P. and Rahman Z. U. (2010) FIB-NanoSIMS-TEM coordinated study of a Wark-Lovering rim in a Vigarano type A CAI. 41st Lunar and Planetary Science Conference. Abstract #1177.
Itoh S., Kojima H. and Yurimoto H. (2004) Petrography and oxygen isotopic compositions in refractory inclusions from CO chondrites. Geochim. Cosmochim. Acta 68, 183–194.
Ireland T. R. and Esat T. M. (1986) Laboratory synthesis of calcium dialuminate and hibonite. 17th Lunar and Planetary Science Conference. pp. 378-379.
Jacobsen B., Yin Q.-Z., Moynier F., Amelin Y., Krot A. N., Nagashima K., Hutcheon I. D. and Palm H. (2008) $^{26}$Al–$^{26}$Mg and $^{207}$Pb–$^{206}$Pb systematics of Allende CAIs: Canonical solar initial $^{26}$Al/$^{27}$Al ratio reinstated. Earth Planet. Sci. Lett. 272, 353–364.
Jacobsen B., Han J., Matzel J. E., Brearley A. J. and Hutcheon I. D. (2014) Oxygen isotope variation in fine-grained CAIs in ALHA 77307: mixing and transport in diverse nebular environments. 77th Annual Meteoritical Society Meeting. Abstract #5414.
Kawasaki N., Park C., Sakamoto N., Park S. Y., Kim H. N., Kuroda M., and Yurimoto H. (2019) Variations in intial 26Al/27Al ratios among fluffy Type A Ca-Al-rich inclusions from reduced CV chondrites. Earth Planet. Sci. Lett. 511, 25-35.
Keller L. P., Needham A. W. and Messenger S. (2013) A FIB/TEM study of a complex Wark–Lovering rim on a Vigarano CAI. 76th Annual Meteoritical Society Meeting. Abstract #5300.
Krot A. N., Nagashima K., van Kooten E. M. M. and Bizzarro M. (2017a) High-temperature

rims around calcium–aluminum-rich inclusions from the CR, CB and CH carbonaceous chondrites. Geochim. Cosmochim. Acta 201, 155-184.
Krot A. N., Nagashima K. and Simon S. B. (2017b) Mineralogically-controlled oxygen-isotope exchange in refractory inclusions from CO carbonaceous chondrites during fluid-rock interaction. 80th Annual Meeting of the Meteoritical Society. Abstract #6056.
Krot A. N., Nagashima K., Fintor K. and Pál-Molnár E. (2019) Evidence for oxygen-isotope exchange in refractory inclusions from Kaba (CV3.1) carbonaceous chondrite during fluid-rock interaction on the CV parent asteroid. Geochim. Cosmochim. Acta 246, 419-435.
LaTourrette T. and Wasserburg G. J. (1998) Mg diffusion in anorthite: Implications for the formation of early solar system planetesimals. Earth Planet. Sci. Lett. 158, 91–108.
LaTourrette T. and Hutcheon I. D. (1999) Mg diffusion in melilite: Thermal histories for CAIs and their parent bodies. 30th Lunar and Planetary Science Conference. Abstract #2003.
Lee M. R., Hutchison R. and Graham A. L. (1996) Aqueous alteration in the matrix of the Vigarano (CV3) carbonaceous chondrite. Meteorit. Planet. Sci. 31, 477-483.
Liu M.-C., McKeegan K. D., Harrison T. M., Jarzebinski G. and Vltava L. (2018) The Hyperion-II radio-frequency oxygen ion source on the UCLA ims1290 ion microprobe: Beam characterization and applications in geochemistry and cosmochemistry. Int. J. of Mass Spectrom. 424, 1-9.
Liu M.-C., Han J., Brearley A. J. and Hertwig, A. T. (2019) Aluminum-26 chronology of dust coagulation and early solar system evolution. Sci. Adv. 5, eaaw3350.
MacPherson G. J., Grossman L., Beckett J. R. and Allen J. M. (1981) Origin of rims on coarse-grained inclusions in the Allende meteorite. Proc. Lunar Planet. Sci. Conf. 12B, 1079-1091.
MacPherson G. J., Paque J. M., Stolper E. and Grossman L. (1984) The origin and significance of reverse zoning in melilite from Allende Type B inclusions. J. Geol. 92, 289–305.
MacPherson G. J., Kita N. T., Ushikubo T., Bullock E. S. and Davis A. M. (2012) Well-resolved variations in the formation ages for Ca–Al-rich inclusions in the early Solar System. Earth Planet. Sci. Lett. 331–332, 43–54.
Matzel J. E. P., Simon J. I., Hutcheon I. D., Jacobsen B., Simon S. B. and Grossman L. (2013) Oxygen isotope measurements of a rare Murchison type A CAI and its rim. 44th Lunar and Planetary Science Conference. Abstract #2632.
Matzel J., Jacobsen B. and Simon J. I. (2015) Aluminum-magnesium chronology of the rim of a Murchison Type A CAI. 78th annual meeting of the Meteoritical Society. Abstract #5372.
Mendybaev R. A., Richter F. M. and Davis A. M. (2006) Crystallization of melilite from CMAS-liquids and the formation of the melilite mantle of Type B1 CAIs: experimental simulations. Geochim. Cosmochim. Acta 70, 2622–2642.
Nagashima M., Armbruster T. and Hainschwang T. (2010) A temperature-dependent structure study of gem-quality hibonite from Myanmar. Mineral. Mag. 74, 871–885.
Podosek F. A., Zinner E. K., MacPherson G. J., Lundberg L. L., Brannon J. C. and Fahey A. J. (1991) Correlated study of initial $^{87}Sr/^{86}Sr$ and Al-Mg isotopic systematics and petrologic properties in a suite of refractory inclusions from the Allende meteorite. Geochim. Cosmochim. Acta 55, 1083-1110.
Pouchou J. L. and Pichoir F. (1984) A new model for quantitative x-ray microanalysis. Part I: Application to the analysis of homogeneous samples. La Recherche Aerospatiale 3, 13–

38.
Richter F. M., Davis A. M., Ebel D. S. and Hashimoto A. (2002) Elemental and isotopic fractionation of Type B calcium-, aluminum-rich inclusions: Experiments, theoretical considerations, and constraints on their thermal evolution. Geochim. Cosmochim. Acta 66, 521–540.
Ruzicka A. (1997) Mineral layers around coarse-grained, Ca–Al-rich inclusions in CV3 carbonaceous chondrites: formation by high-temperature metasomatism. J. Geophys. Res. 102, 13387–13402.
Ryerson F. J. and McKeegan K. D. (1994) Determination of oxygen self-diffusion in akermanite, anorthite, diopside, and spinel: implications for oxygen isotopic anomalies and the thermal histories of Ca–Al-rich inclusions. Geochim. Cosmochim. Acta 58, 3713–3734.
Schmid H. and De Jonghe L. C. (1983) Structure and nonstoichiometry of calcium aluminates. Philos. Mag. A 48, 287–297.
Simon J. I. and DePaolo D. J. (2010) Stable calcium isotopic composition of meteorites and rocky planets. Earth Planet. Sci. Lett. 289, 457-466.
Simon J. I. and Young E. D. (2011) Resetting, errorchrons and the meaning of canonical CAI initial $^{26}Al/^{27}Al$ values. Earth Planet. Sci. Lett. 304, 468-482.
Simon J. I., Young E. D., Russell S. S., Tonui E. K., Dyl K. A. and Manning C. E. (2005) A short timescale for changing oxygen fugacity in the solar nebula revealed by high-resolution $^{26}Al$–$^{26}Mg$ dating of CAI rims. Earth Planet. Sci. Lett. 238, 272– 283.
Simon J. I., Hutcheon I. D., Simon S. B., Matzel J. E. P., Ramon E. C., Weber P. K., Grossman L. and DePaolo D. J. (2011) Oxygen isotope variations at the margin of a CAI records circulation within the solar nebula. Science 331, 1175–1178.
Simon J. I., Matzel J. E. P., Simon S. B., Hutcheon I. D., Ross D. K, Weber P. K. and Grossman L. (2016) Oxygen isotopic variations in the outer margins and Wark–Lovering rims of refractory inclusions. Geochim. Cosmochim. Acta 186, 242-276.
Simon S. B. and Grossman L. (2006) A comparative study of melilite and fassaite in Type B1 and B2 refractory inclusions. Geochim. Cosmochim. Acta 70, 7780-798.
Simon S. B., Yoneda S., Grossman L. and Davis A. M. (1994) A $CaAl_4O_7$-bearing refractory spherule from Murchison: Evidence for very high-temperature melting in the solar nebula. Geochim. Cosmochim. Acta 58, 1937-1949.
Simon S. B., Davis A. M. and Grossman L. (1999) Origin of compact Type A refractory inclusions from CV3 carbonaceous chondrites. Geochim. Cosmochim. Acta 63, 1233-1248.
Simon S. B., Sutton S. R. and Grossman L. (2007) Valence of titanium and vanadium in pyroxene in refractory inclusion interiors and rims. Geochim. Cosmochim. Acta 71, 3098-3118.
Slodzian G., Hillion F., Stadermann F. J. and Zinner E. (2004) QSA influences on isotopic ratio measurements. Appl. Surf. Sci. 231, 874–877.
Stolper E. (1982) Crystallization sequences of Ca–Al-rich inclusions from Allende: an experimental study. Geochim. Cosmochim. Acta 46, 2159–2180.
Taylor D. J., McKeegan K. D. and Krot A. N. (2005) High-resolution $^{26}Al$ Chronology: Resolved time interval between rim and interior of a highly fractionated compact type A CAI from Efremovka. 36th Lunar and Planetary Science conference. Abstract #2121.
Toppani A., Paque J. M., Burnett D. S., Teslich N., Moberlychan W., Dai Z. R., and Bradley J. P. (2006) Wark-Lovering rims at the nanometer scale: A transmission electron

microscopy study. 37th Lunar and Planetary Science. Abstract #2030.
Ushikubo T., Tenner T. J., Hiyagon H. and Kita N. T. (2017) A long duration of the $^{16}$O-rich reservoir in the solar nebula, as recorded in fine-grained refractory inclusions from the least metamorphosed carbonaceous chondrites. Geochim. Cosmochim. Acta 201, 103-122.
Villeneuve J., Chaussidon M. and Libourel G. (2009) Homogeneous distribution of $^{26}$Al in the solar system from the Mg isotopic composition of chondrules. Science 325, 985–988.
Wang J., Davis A. M., Clayton R. N., Mayeda T. K. and Hashimoto A. (2001) Chemical and isotopic fractionation during the evaporation of the FeO-MgO-$SiO_2$-CaO-$Al_2O_3$-$TiO_2$-REE melt system. Geochim. Cosmochim. Acta 65, 479–494.
Wark D. and Lovering J. F. (1977) Marker events in the early evolution of the solar system: evidence from rims on Ca–Al-rich inclusions in carbonaceous chondrites. Proc. Lunar Planet. Sci. Conf. 8, 95–112.
Wark D. A. and Boynton W. V. (2001) The formation of rims on calcium–aluminum-rich inclusions: Step I Flash heating. Meteorit. Planet. Sci. 36, 1135–1166.
Wasson J. T., Yurimoto H. and Russell S. S. (2001) $^{16}$O-rich melilite in CO3.0 chondrites: Possible formation of common, $^{16}$O-poor melilite by aqueous alteration. Geochim. Cosmochim. Acta 65, 4539–4549.
Weber D. and Bischoff A. (1994) The occurrence of grossite ($CaAl_4O_7$) in chondrites. Geochim. Cosmochim. Acta 58, 3855-3877.
Yoneda S. and Grossman L. (1995) Condensation of CaO–MgO–$Al_2O_3$–$SiO_2$ liquids from cosmic gases. Geochim. Cosmochim. Acta 59, 3413–3444.
Yoshitake M., Koide Y. and Yurimoto H. (2005) Correlations between oxygen-isotopic composition and petrologic setting in a coarse-grained Ca, Al–rich inclusion. Geochim. Cosmochim. Acta 69, 2663–2674.
Young E. D.and Russell S. S. (1998) Oxygen Reservoirs in the Early Solar Nebula Inferred from an Allende CAI. Science 282, 452-455.
Young E. D., Simon J. I., Galy A., Russell S. S., Tonui E. and Lovera O. (2005) Supra-canonical $^{26}$Al/$^{27}$Al and the residence time of CAIs in the solar protoplanetary disk. Science 308, 223-227.
Zega T. J., Cosarinsky M., Stroud R. M. and McKeegan K. D. (2007) FIB-TEM study of a Wark-Lovering rim in an Allende Type-A CAI. 70th Annual Meteoritical Society Meeting. Abstract #5289.
Zega T. J., Cosarinsky M., MacPherson G. J. and McKeegan K. D. (2009) FIB-TEM analysis on a Wark-Lovering rim from the Vigarano CV3 chondrite. 72nd Annual Meteoritical Society Meeting. Abstract #5374.
Zega T. J., Simon S. B. and Grossman L. (2010) Microstructural analysis of a Wark-Lovering rim around an Allende CAI. 73rd Annual Meteoritical Society Meeting. Abstract #5433.

## TABLES

**Table 1.** EPMA data (wt%) of the WL rim minerals from the Vigarano CAI *Big Guy*.

| mineral | hibonite | | spinel | | melilite | | pyroxene | | | | | |
|---|---|---|---|---|---|---|---|---|---|---|---|---|
| | average | SD* | average | SD | average | SD | top | ↔ | | | | base |
| No. of analyses | 23 | | 20 | | 3 | | | | | | | |
| $SiO_2$ | 0.26 | 0.16 | 0.08 | 0.03 | 23.22 | 0.83 | 37.58 | 45.48 | 49.06 | 50.77 | 52.83 | 55.54 |
| $TiO_2$ | 4.20 | 0.71 | 0.23 | 0.03 | 0.07 | 0.01 | 2.23 | 3.44 | 1.71 | 1.25 | 0.30 | 0.05 |
| $Al_2O_3$ | 84.55 | 1.49 | 71.04 | 0.34 | 34.01 | 0.56 | 26.95 | 12.44 | 7.73 | 5.42 | 3.16 | 0.54 |
| $V_2O_3$ | 0.03 | 0.03 | 0.15 | 0.03 | 0.01 | 0.00 | 0.02 | 0.00 | 0.02 | 0.06 | 0.00 | 0.03 |
| $Cr_2O_3$ | 0.01 | 0.01 | 0.22 | 0.02 | 0.00 | 0.01 | 0.22 | 0.12 | 0.16 | 0.10 | 0.07 | 0.01 |
| FeO | 0.42 | 0.77 | 0.63 | 0.28 | 0.18 | 0.03 | 1.13 | 0.26 | 0.21 | 0.43 | 0.59 | 0.28 |
| MnO | 0.01 | 0.01 | 0.01 | 0.02 | 0.01 | 0.01 | 0.00 | 0.00 | 0.02 | 0.00 | 0.00 | 0.00 |
| MgO | 2.22 | 0.30 | 28.10 | 0.24 | 1.34 | 0.07 | 7.89 | 12.86 | 14.98 | 16.26 | 18.37 | 19.01 |
| CaO | 8.40 | 0.15 | 0.12 | 0.04 | 40.28 | 0.35 | 24.47 | 25.37 | 25.56 | 25.48 | 25.37 | 25.39 |
| $Na_2O$ | 0.02 | 0.03 | 0.01 | 0.01 | 0.03 | 0.02 | 0.02 | 0.00 | 0.03 | 0.01 | 0.02 | 0.00 |
| Total | 100.12 | | 100.59 | | 99.15 | | 100.51 | 99.97 | 99.48 | 99.78 | 100.71 | 100.85 |
| | | | | | | | | | | | | |
| Si | 0.030 | | 0.002 | | 1.069 | | 1.363 | 1.656 | 1.790 | 1.845 | 1.900 | 1.984 |
| Ti | 0.355 | | 0.004 | | 0.002 | | 0.061 | 0.094 | 0.047 | 0.034 | 0.008 | 0.002 |
| Al | 11.199 | | 1.981 | | 1.846 | | 1.153 | 0.534 | 0.332 | 0.232 | 0.134 | 0.023 |
| V | 0.002 | | 0.003 | | - | | 0.001 | - | 0.001 | 0.002 | - | 0.001 |
| Cr | 0.001 | | 0.004 | | - | | 0.006 | 0.004 | 0.005 | 0.003 | 0.002 | 0.000 |
| Fe | 0.040 | | 0.012 | | 0.007 | | 0.034 | 0.008 | 0.006 | 0.013 | 0.018 | 0.009 |
| Mn | 0.001 | | - | | - | | - | - | 0.001 | - | - | - |
| Mg | 0.372 | | 0.991 | | 0.092 | | 0.427 | 0.698 | 0.815 | 0.881 | 0.985 | 1.013 |
| Ca | 1.011 | | 0.003 | | 1.987 | | 0.951 | 0.990 | 0.999 | 0.992 | 0.978 | 0.972 |
| Na | 0.004 | | - | | 0.003 | | 0.002 | - | 0.002 | 0.001 | 0.001 | - |
| Total | 13.015 | | 3.000 | | 5.006 | | 3.998 | 3.984 | 3.998 | 4.003 | 4.026 | 4.004 |
| No. of oxygen anions | 19 | | 4 | | 7 | | 6 | 6 | 6 | 6 | 6 | 6 |
| Åk (mol%) | | | | | 9.1 | | | | | | | |

* Standard deviation (1σ).

**Table 2.** Average TEM EDX data of the WL rim minerals from the Vigarano CAI *Big Guy*.

| mineral | melilite[1] | grossite | hibonite | perovskite | spinel | melilite[2] | melilite[3] | anorthite | pyroxene[1] | pyroxene[2] | pyroxene[3] | pyroxene[4] | olivine |
|---|---|---|---|---|---|---|---|---|---|---|---|---|---|
| No. of analyses | 8 | 3 | 31 | 3 | 7 | 9 | 12 | 4 | 3 | 20 | 10 | 6 | 7 |
| $SiO_2$ | 19.30 | - | - | 0.22 | 0.15 | 23.85 | 22.5 | 41.94 | 27.09 | 37.98 | 44.98 | 56.25 | 44.77 |
| $TiO_2$ | - | - | 5.27 | 55.43 | 0.06 | - | 0.02 | - | 14.09 | 4.79 | 4.80 | 0.19 | - |
| $Al_2O_3$ | 36.92 | 77.25 | 84.67 | 0.57 | 72.69 | 33.41 | 34.74 | 37.10 | 29.24 | 23.45 | 17.24 | 0.60 | - |
| $V_2O_3$ | - | - | - | - | 0.18 | - | 0.01 | - | - | - | - | - | - |
| $Cr_2O_3$ | - | - | - | - | 0.18 | - | - | - | - | - | - | - | - |
| FeO | 0.03 | - | 0.02 | - | 0.71 | 0.02 | - | - | 0.27 | 0.21 | 0.22 | 0.49 | 2.56 |
| MgO | - | - | 0.99 | 0.07 | 25.94 | 0.47 | 0.16 | - | 2.40 | 6.33 | 7.22 | 15.70 | 52.61 |
| CaO | 43.75 | 22.71 | 9.05 | 43.70 | 0.07 | 42.24 | 42.58 | 20.96 | 26.91 | 27.22 | 25.54 | 26.77 | 0.06 |
| Total | 100.00 | 99.96 | 100.00 | 99.99 | 99.98 | 99.99 | 100.01 | 100.00 | 100.00 | 99.98 | 100.00 | 100.00 | 100.00 |
| | | | | | | | | | | | | | |
| Si | 0.895 | - | - | 0.005 | 0.004 | 1.093 | 1.033 | 1.951 | 1.018 | 1.394 | 1.625 | 2.029 | 1.052 |
| Ti | - | - | 0.446 | 0.949 | 0.001 | - | 0.001 | - | 0.398 | 0.132 | 0.13 | 0.005 | - |
| Al | 2.021 | 3.96 | 11.232 | 0.015 | 2.031 | 1.804 | 1.882 | 2.035 | 1.295 | 1.015 | 0.736 | 0.025 | - |
| V | - | - | - | - | 0.003 | - | 0 | - | - | - | - | - | - |
| Cr | - | - | - | - | 0.003 | - | - | - | - | - | - | - | - |
| Fe | 0.001 | - | 0.002 | - | 0.014 | 0.001 | - | - | 0.008 | 0.006 | 0.007 | 0.015 | 0.051 |
| Mg | - | - | 0.166 | 0.003 | 0.917 | 0.032 | 0.011 | - | 0.134 | 0.347 | 0.389 | 0.845 | 1.843 |
| Ca | 2.178 | 1.058 | 1.091 | 1.066 | 0.002 | 2.074 | 2.099 | 1.047 | 1.084 | 1.071 | 0.99 | 1.035 | 0.002 |
| Total | 5.095 | 5.018 | 12.937 | 2.038 | 2.975 | 5.004 | 5.026 | 5.033 | 3.937 | 3.965 | 3.877 | 3.954 | 2.948 |
| No. of oxygen anions | 7 | 7 | 19 | 3 | 4 | 7 | 7 | 8 | 6 | 6 | 6 | 6 | 4 |
| Fe×100 /(Fe+Mg) | | | | | 1.5 | | | | | | | | 2.7 |
| Åk (mol%) | 0 | | | | | 3.5 | 1.1 | | | | | | |

*Melilite 1: melilite in the mantle edge, just below the hibonite layer; 2: melilite in contact with pyroxene, without anorthite; 3: melilite in contact with anorthite.

*Pyroxene 1: pyroxene present between spinel and melilite; 2: pyroxene in contact with melilite, without anorthite; 3: pyroxene in contact with anorthite; 4: diopside intergrown with forsteritic olivine in the outermost pyroxene layer.

**Table 3.** Oxygen isotopic compositions of individual WL rim minerals from the Vigarano CAI *Big Guy*, obtained using NanoSIMS.

| mineral | spot # | $\delta^{18}O$ | 2σ | $\delta^{17}O$ | 2σ | $\Delta^{17}O$ | 2σ |
|---|---|---|---|---|---|---|---|
| **core** | | | | | | | |
| spinel | 1 | −45.9 | 1.0 | −47.8 | 2.2 | −23.9 | 3.2 |
| spinel | 2 | −44.7 | 1.0 | −47.4 | 2.2 | −24.2 | 3.2 |
| spinel | 3 | −42.8 | 2.2 | −47.2 | 5.0 | −25.0 | 7.1 |
| Al,Ti-diopside | 4 | −23.7 | 1.9 | −27.2 | 4.4 | −14.9 | 6.4 |
| Al,Ti-diopside | 5 | −20.7 | 0.9 | −28.0 | 2.0 | −17.2 | 2.9 |
| Al,Ti-diopside | 6 | −18.6 | 1.9 | −28.9 | 4.4 | −19.3 | 6.3 |
| **mantle** | | | | | | | |
| melilite | 15 | 19.6 | 0.9 | 9.7 | 2.2 | −0.5 | 3.1 |
| melilite | 16 | 15.4 | 1.0 | 1.3 | 2.2 | −6.7 | 3.2 |
| melilite | 17 | 14.1 | 1.0 | 0.8 | 2.2 | −6.5 | 3.2 |
| melilite | 18 | 19.0 | 0.9 | 10.2 | 2.0 | 0.3 | 2.9 |
| melilite | 19 | 15.4 | 1.0 | 9.2 | 2.2 | 1.2 | 3.1 |
| melilite | 20 | 14.0 | 1.0 | 4.0 | 2.2 | −3.2 | 3.2 |
| melilite | 21 | 0.7 | 0.9 | −9.0 | 2.0 | −9.3 | 2.9 |
| melilite | 22 | 5.2 | 1.0 | −2.1 | 2.2 | −4.8 | 3.2 |
| melilite | 23 | 4.6 | 1.0 | −1.7 | 2.2 | −4.1 | 3.2 |
| melilite | 24 | −12.8 | 2.0 | −17.3 | 4.6 | −10.7 | 6.7 |
| melilite | 25 | 0.6 | 1.0 | −9.3 | 2.2 | −9.6 | 3.2 |
| melilite | 26 | −22.6 | 2.1 | −33.2 | 4.7 | −21.5 | 6.8 |
| melilite | 28 | −19.4 | 2.0 | −28.3 | 4.7 | −18.2 | 6.8 |
| melilite | 29 | −19.0 | 2.0 | −29.6 | 4.7 | −19.7 | 6.7 |
| melilite | 31 | −18.3 | 0.9 | −23.4 | 2.0 | −13.9 | 2.9 |
| melilite | 32 | −2.9 | 1.0 | −9.1 | 2.2 | −7.6 | 3.2 |
| melilite | 33 | −6.6 | 1.9 | −17.4 | 4.4 | −13.9 | 6.3 |
| melilite | 34 | 5.7 | 0.9 | 1.1 | 2.0 | −1.9 | 2.9 |
| melilite | 35 | 4.8 | 0.9 | −4.2 | 2.0 | −6.7 | 2.9 |
| melilite | 36 | −5.0 | 0.9 | −11.1 | 2.0 | −8.5 | 2.9 |
| melilite | 37 | −0.8 | 0.9 | −7.3 | 2.0 | −6.9 | 2.9 |
| melilite | 38 | −9.6 | 0.9 | −15.9 | 2.0 | −10.9 | 2.8 |
| spinel | 27 | −37.9 | 1.0 | −40.4 | 2.4 | −20.8 | 3.4 |
| spinel | 30 | −38.0 | 1.0 | −41.8 | 2.4 | −22.1 | 3.4 |
| **WL rim** | | | | | | | |
| hibonite | 39 | −50.7 | 0.9 | −49.4 | 2.1 | −23.0 | 3.0 |
| hibonite | 40 | −50.7 | 0.9 | −52.0 | 2.1 | −25.7 | 3.1 |
| spinel | 41 | −50.7 | 0.9 | −52.0 | 2.1 | −25.7 | 3.1 |
| spinel | 42 | −45.7 | 1.0 | −46.8 | 2.2 | −23.0 | 3.2 |
| spinel | 43 | −40.8 | 2.3 | −47.5 | 5.2 | −26.3 | 7.4 |
| melilite | 45 | −38.7 | 1.0 | −40.1 | 2.2 | −20.0 | 3.1 |
| anorthite | 46 | −36.6 | 0.9 | −40.8 | 2.1 | −21.8 | 3.1 |
| diopside | 47 | −40.0 | 0.9 | −41.7 | 2.1 | −20.9 | 3.0 |
| diopside | 48 | −40.0 | 0.9 | −41.8 | 2.1 | −21.0 | 3.1 |
| diopside | 49 | −38.5 | 1.0 | −42.9 | 2.2 | −22.9 | 3.2 |

Table 4. Magnesium isotopic compositions of individual WL rim minerals from the Vigarano CAI *Big Guy*, obtained using the ims-1290 ion microprobe.

| mineral | spot # | $^{27}Al/^{24}Mg$ | 2σ | $\Delta^{26}Mg^*$ (‰) | 2σ | $\delta^{25}Mg$ (‰) | 2σ | | mineral | spot # | $^{27}Al/^{24}Mg$ | 2σ | $\Delta^{26}Mg^*$ (‰) | 2σ | $\delta^{25}Mg$ (‰) | 2σ |
|---|---|---|---|---|---|---|---|---|---|---|---|---|---|---|---|---|
| multicollection | | | | | | | | | monocollection | | | | | | | |
| **Core** | | | | | | | | | **Mantle** | | | | | | | |
| spinel | s1 | 2.50 | 0.01 | 0.96 | 0.13 | 9.02 | 0.06 | | melilite | m1 | 22.01 | 0.04 | 7.96 | 2.33 | 9.20 | 1.04 |
| | s2 | 2.52 | 0.01 | 1.04 | 0.15 | 9.56 | 0.06 | | | m2** | 10.69 | 0.19 | -0.69 | 3.13 | 3.94 | 1.21 |
| | s3 | 2.52 | 0.01 | 0.89 | 0.15 | 9.63 | 0.06 | | | m3** | 24.67 | 0.05 | 5.74 | 2.07 | 3.99 | 0.93 |
| | s4 | 2.53 | 0.01 | 0.91 | 0.13 | 9.30 | 0.05 | | | m4 | 2.73 | 0.01 | -1.78 | 1.97 | 13.85 | 0.80 |
| | s5 | 2.53 | 0.01 | 1.08 | 0.17 | 9.11 | 0.07 | | | m5 | 20.87 | 0.12 | 10.78 | 5.03 | 10.92 | 2.08 |
| | s6 | 2.55 | 0.01 | 1.05 | 0.19 | 9.40 | 0.09 | | | m6 | 18.03 | 0.08 | 7.10 | 3.00 | 9.88 | 1.31 |
| | s7 | 2.54 | 0.01 | 0.86 | 0.14 | 9.27 | 0.06 | | | m7 | 4.14 | 0.02 | 0.55 | 2.18 | 12.52 | 0.80 |
| | s8 | 2.53 | 0.01 | 0.97 | 0.13 | 9.10 | 0.05 | | | m8 | 5.44 | 0.02 | -0.85 | 2.08 | 12.76 | 0.82 |
| Al,Ti-diopside | f1 | 2.82 | 0.01 | 0.80 | 0.31 | 9.39 | 0.13 | | | m9 | 15.84 | 0.05 | 6.11 | 2.38 | 10.39 | 0.96 |
| | f2 | 3.11 | 0.01 | 1.22 | 0.36 | 8.90 | 0.14 | | | m10 | 15.36 | 0.04 | 3.90 | 2.27 | 10.34 | 0.89 |
| | f3 | 2.39 | 0.01 | 1.04 | 0.31 | 8.69 | 0.13 | | | m11 | 18.17 | 0.07 | 6.82 | 2.99 | 9.87 | 1.29 |
| | f4 | 2.47 | 0.01 | 0.95 | 0.37 | 9.12 | 0.16 | | | m12 | 18.17 | 0.05 | 4.93 | 2.49 | 9.55 | 1.10 |
| | f5 | 2.79 | 0.01 | 1.03 | 0.36 | 8.90 | 0.16 | | | m13 | 19.66 | 0.11 | 8.82 | 2.99 | 8.77 | 1.26 |
| | f6 | 2.87 | 0.01 | 0.70 | 0.30 | 9.04 | 0.13 | | | m14 | 11.91 | 0.02 | 3.55 | 1.77 | 8.92 | 0.72 |
| | f7 | 2.14 | 0.01 | 0.67 | 0.34 | 9.34 | 0.14 | | | m15 | 14.82 | 0.02 | 6.45 | 2.51 | 8.57 | 1.13 |
| **Mantle** | | | | | | | | | | m16 | 20.28 | 0.03 | 5.61 | 2.45 | 9.90 | 1.04 |
| spinel | s9 | 2.53 | 0.01 | 1.05 | 0.13 | 9.19 | 0.05 | | | m17 | 23.98 | 0.11 | 6.43 | 2.46 | 8.65 | 1.10 |
| | s10 | 2.59 | 0.01 | 1.06 | 0.13 | 8.91 | 0.05 | | | m18** | 35.74 | 0.28 | 11.77 | 3.44 | 5.30 | 1.45 |
| | s11 | 2.69 | 0.01 | 1.11 | 0.18 | 9.24 | 0.07 | | | m19 | 18.39 | 0.02 | 6.70 | 2.48 | 8.62 | 0.98 |
| | s12 | 2.55 | 0.01 | 1.10 | 0.11 | 9.46 | 0.05 | | | m20 | 2.30 | 0.06 | -4.08 | 3.52 | 18.96 | 1.38 |
| | s13 | 2.56 | 0.01 | 1.04 | 0.13 | 9.14 | 0.04 | | | m21 | 1.97 | 0.05 | -3.09 | 4.96 | 17.01 | 1.60 |
| | s14 | 2.67 | 0.01 | 1.22 | 0.11 | 9.33 | 0.04 | | | m22 | 1.99 | 0.04 | -2.47 | 4.39 | 17.28 | 1.79 |
| hibonite | h2* | 20.35 | 0.02 | 7.34 | 0.57 | 6.52 | 0.23 | | | m23 | 2.00 | 0.03 | -3.92 | 2.17 | 16.07 | 0.96 |
| | h3 | 19.56 | 0.02 | 7.12 | 0.40 | 7.27 | 0.15 | | | m24 | 2.16 | 0.02 | -3.50 | 3.18 | 14.77 | 1.09 |
| **WL rim** | | | | | | | | | | m25 | 3.33 | 0.03 | -1.71 | 3.10 | 13.28 | 1.25 |
| hibonite | h1 | 12.25 | 0.02 | 4.62 | 0.38 | -3.27 | 0.15 | | | m26 | 5.20 | 0.03 | -0.20 | 3.08 | 11.52 | 1.39 |
| | h4 | 23.62 | 0.02 | 8.38 | 0.45 | 2.87 | 0.18 | | | m27 | 5.14 | 0.06 | -0.29 | 3.47 | 13.32 | 1.54 |
| | h5 | 36.78 | 0.03 | 13.48 | 0.74 | -2.08 | 0.30 | | | m28 | 4.81 | 0.03 | 0.46 | 2.03 | 11.97 | 0.74 |
| | h6 | 33.67 | 0.04 | 11.73 | 0.52 | -1.51 | 0.19 | | | m29 | 6.49 | 0.03 | 0.80 | 3.65 | 11.63 | 1.62 |
| | h7 | 29.73 | 0.14 | 10.51 | 0.61 | -0.97 | 0.27 | | | m30 | 14.25 | 0.06 | 4.08 | 4.39 | 10.25 | 1.83 |
| | h8* | 8.23 | 0.01 | 2.93 | 0.27 | -1.57 | 0.12 | | | m31 | 16.39 | 0.07 | 4.48 | 5.66 | 11.13 | 2.60 |
| spinel | s15 | 2.69 | 0.01 | 0.87 | 0.14 | -0.84 | 0.06 | | | m32 | 16.34 | 0.07 | 6.02 | 6.41 | 11.36 | 2.67 |
| | s16* | 3.22 | 0.01 | 1.21 | 0.17 | -1.45 | 0.07 | | | m33 | 17.50 | 0.08 | 3.34 | 5.65 | 13.55 | 2.32 |
| | s17* | 3.98 | 0.03 | 1.39 | 0.24 | -1.66 | 0.11 | | | m34 | 55.12 | 0.69 | 15.44 | 6.96 | 10.51 | 3.17 |
| | s19 | 2.62 | 0.01 | 1.17 | 0.13 | -1.52 | 0.05 | | | m35 | 35.80 | 0.49 | 11.78 | 3.99 | 13.92 | 1.64 |

| | | | | | | | | | | | | | | | | |
|---|---|---|---|---|---|---|---|---|---|---|---|---|---|---|---|---|
| diopside | d1 | 0.43 | 0.01 | 0.22 | 0.25 | -0.07 | 0.11 | | **WL rim** | | | | | | | |
| | d4 | 0.33 | 0.01 | -0.10 | 0.22 | 1.60 | 0.09 | | anorthite | a1 | 57.57 | 2.43 | 0.55 | 6.98 | 4.57 | 2.75 |
| | | | | | | | | | | a2 | 10.40 | 0.15 | -2.54 | 3.26 | 6.67 | 1.24 |
| | | | | | | | | | | a3 | 13.67 | 0.49 | -1.97 | 4.71 | 6.35 | 1.84 |

* Minor overlapping with melilite (h2 and h8) or hibonite (s16 and s17). ** m2, m3, and m18 are within a ~5 μm distance of the hibonite layer.

## FIGURES

**Figure 1.** BSE images (a, b) and combined X-ray elemental map (c) in Mg (red), Ca (green), and Al (blue) of the Vigarano CAI *Big Guy*. The CAI has a core-mantle-rim structure, as separated by the dashed lines in (a). The region outlined in (a) is shown in detail in (b, c). This inclusion has a complete multi-layered WL rim mineral sequence (from inside outwards): (1) gehlenite in the mantle edge, (2) hibonite, (3) spinel with hibonite and perovskite inclusions, (4) gehlenitic melilite, (5) anorthite, (6) zoned diopside, and finally (7) forsteritic olivine intergrown with diopside. The solid line in (a) indicates the EPMA traverse across a single melilite crystal shown in Figure 2c. Abbreviations hereafter: hib = hibonite; pv = perovskite; sp = spinel; mel = melilite; an = anorthite; di = diopside; fo = forsterite; WL = Wark-Lovering rim; AR = accretionary rim.

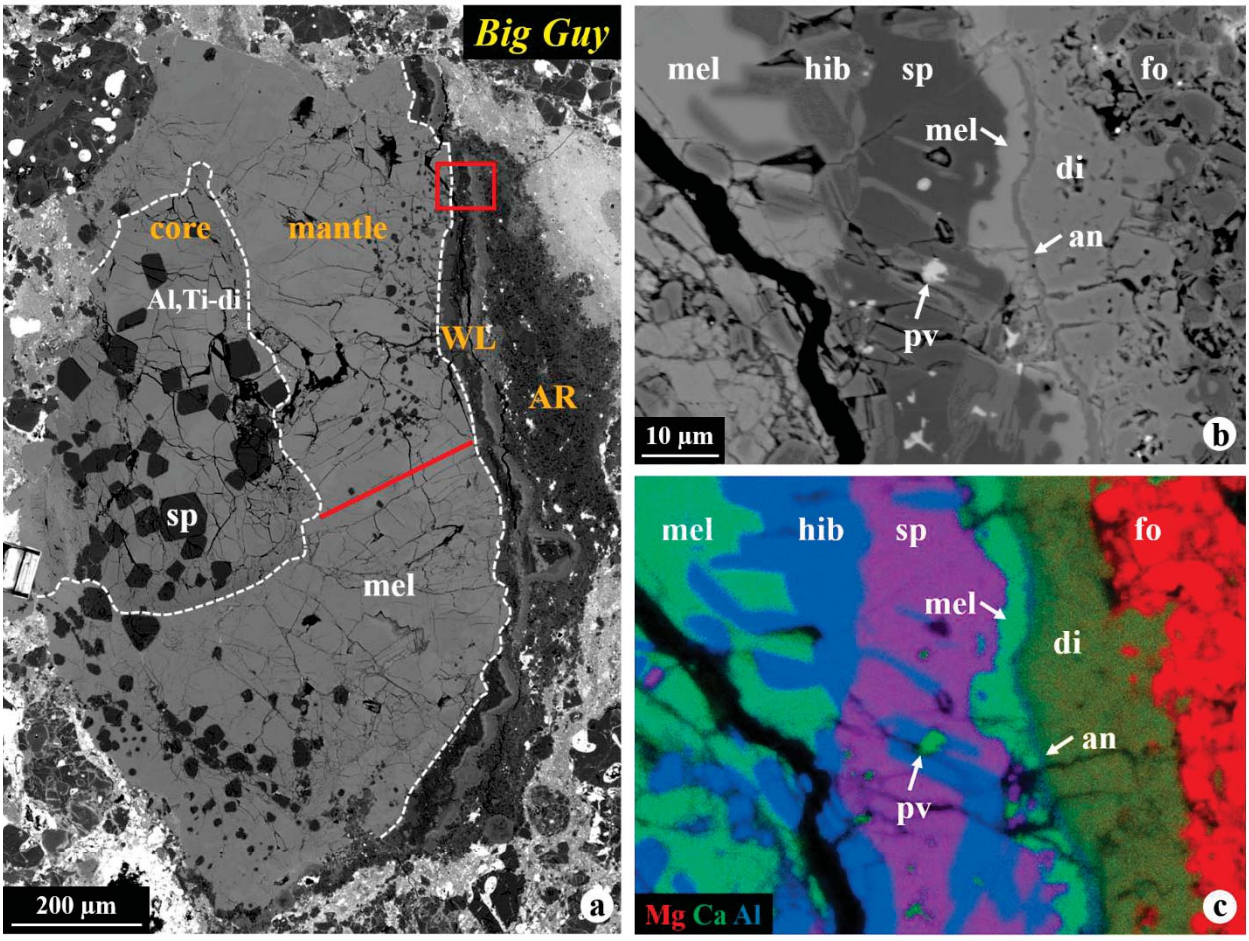


**Figure 2.** (a, b) BF STEM images of the CAI mantle edge composed of oriented gehlenite with minor fine-grained inclusions of hibonite and grossite. An inset in (a) is electron diffraction

patterns of melilite view down the [130] zone axis, whereas an inset in (b) is electron diffraction patterns of grossite view down the [$\bar{3}\bar{1}2$] zone axis. (c) Compositional profile across a single melilite crystal in the CAI mantle, obtained using EPMA. The traverse was obtained along the elongation direction of the melilite crystal with a spacing of 2 μm between points. See Figure 1 for the location of the traverse line. Abbreviation: grs = grossite.

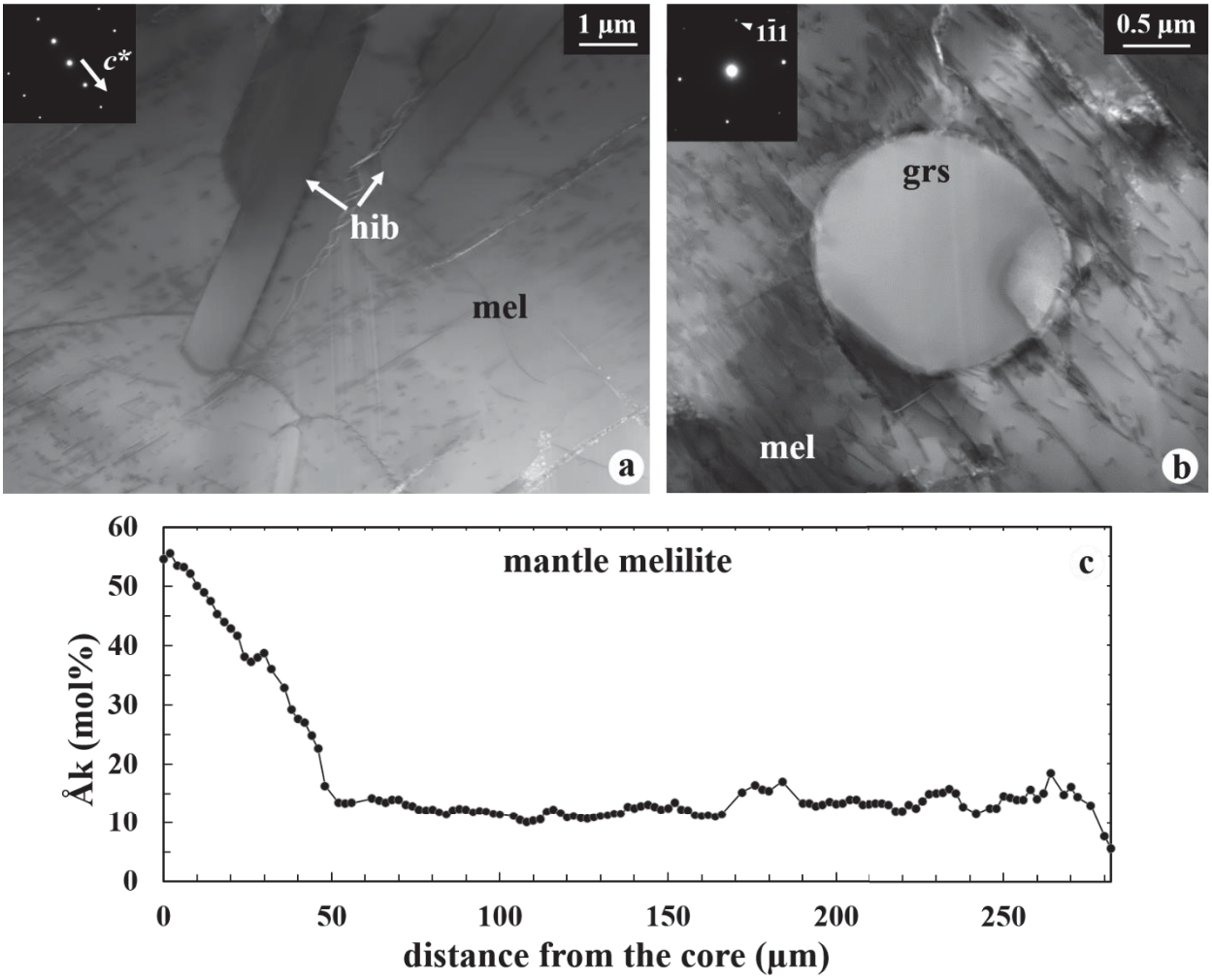


**Figure 3.** BF STEM image of compactly-intergrown hibonite laths with minor melilite inclusions. The inset electron diffraction patterns are taken from an outlined region in hibonite with the beam parallel to the [110] zone axis.

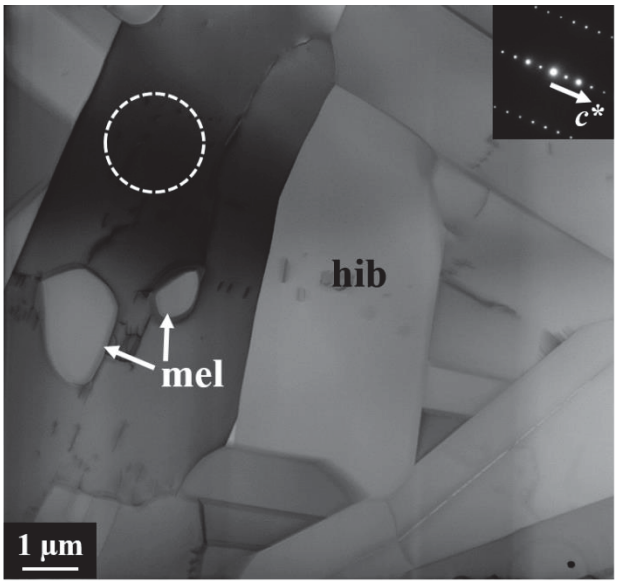


**Figure 4.** (a) BF STEM image of highly curved hibonite-spinel interface, as outlined by the dotted line. (b) BSE image of platy spinel at the interface with the CAI mantle. (c) BF STEM image of defect-structured hibonite inclusion in spinel that contains elongated spinel. (d) BF STEM image of elongated perovskite surrounded by spinel. The twinning planes in perovskite, indicated by arrows, are apparent. (e) HR TEM image of hibonite that consists of irregular intergrowths of 2.6 nm (001) spacing within 2.2 nm (001) spacing. The inset Fast Fourier Transform patterns, indexed as the [$1\bar{1}0$] zone axis, show strong streaking along $c^*$, consistent with the presence of stacking defects. (f) Electron diffraction patterns of perovskite, showing a twin relationship between the [100] and [001] zones. Reflections from the [001] zone are indicated by arrows. (g, h) Electron diffraction patterns of spinel and perovskite, taken from areas outlined in (d), indicating a crystallographic orientation relationship between these two phases.

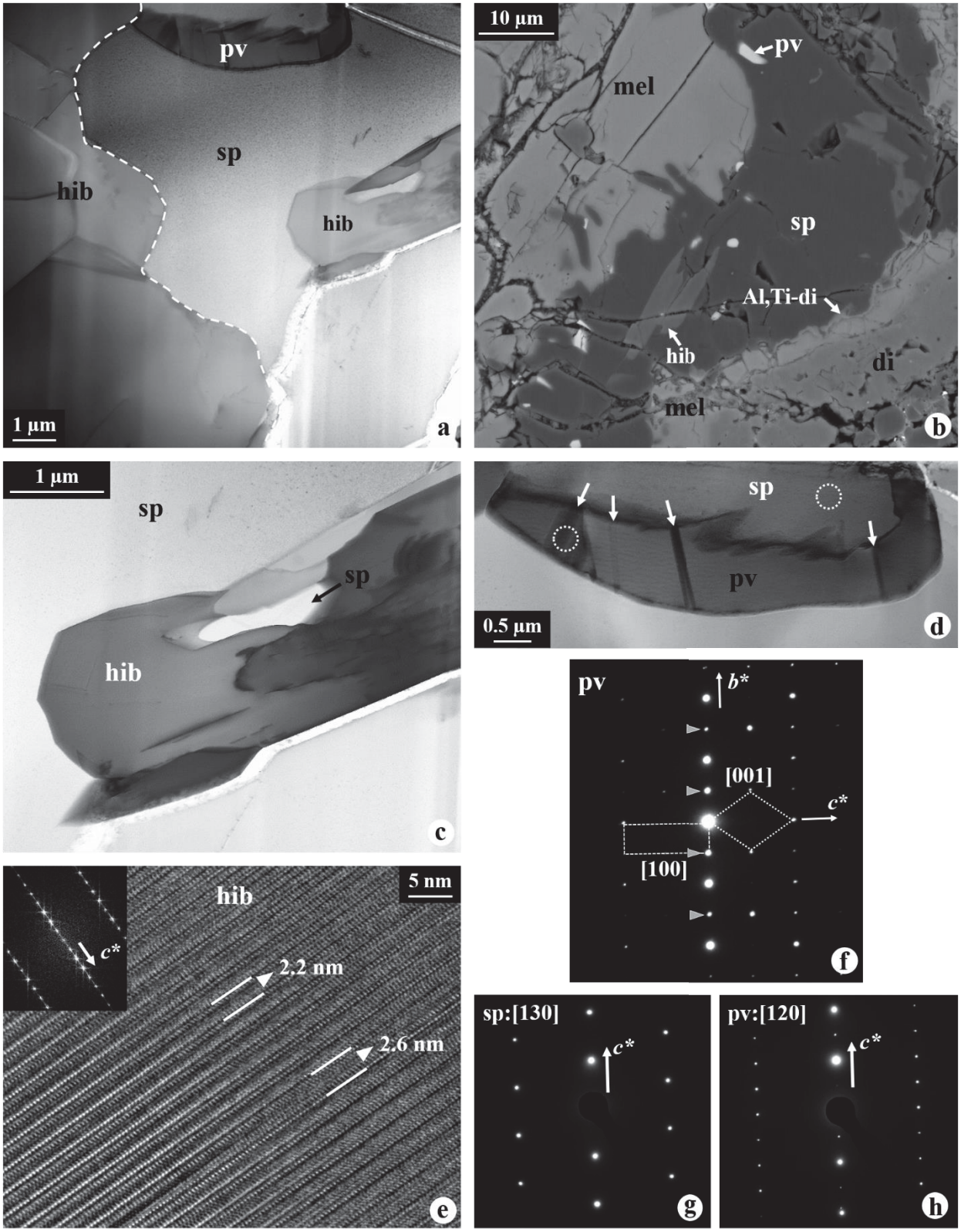


**Figure 5.** BF STEM images (a, b) and corresponding combined X-ray elemental maps (c, d) in

Ti (red), Ca (green), and Al (blue) of the WL rim layers from spinel to diopside, as seperated by the dashed lines. In (a, c), no anorthite is observed between melilite and diopside, and Al,Ti-rich diopside is locally present onto spinel. Fe-rich amorphous materials are present along the grain boundaries and cracks. Fine-grained spinel, indicated by arrows, are included in diopside and melilite (c) and anorthite (d). (e) Mg profile across the melilite layer, extracted from the TEM EDX spectrum images outlined in (b). The vertical dotted line in (e) represents a grain boundary between melilite and anorthite, respectively. (f, g) Al, Ti, and Mg profiles across the diopside layer, extracted from the TEM EDX spectrum images outlined in (a, b). The vertical dotted lines in (f, g) represent diopside grain boundaries with melilite and anorthite, respectively. In these profiles, 0 μm is indicated in (a, c). Diopside is zoned in Al and Ti regardless of whether or not it is in direct contact with melilite. However, diopside next to melilite contains higher $Al_2O_3$ contents and slightly lower MgO contents, compared to that next to anorthite. Abbreviation: am = Fe-rich amorphous materials.

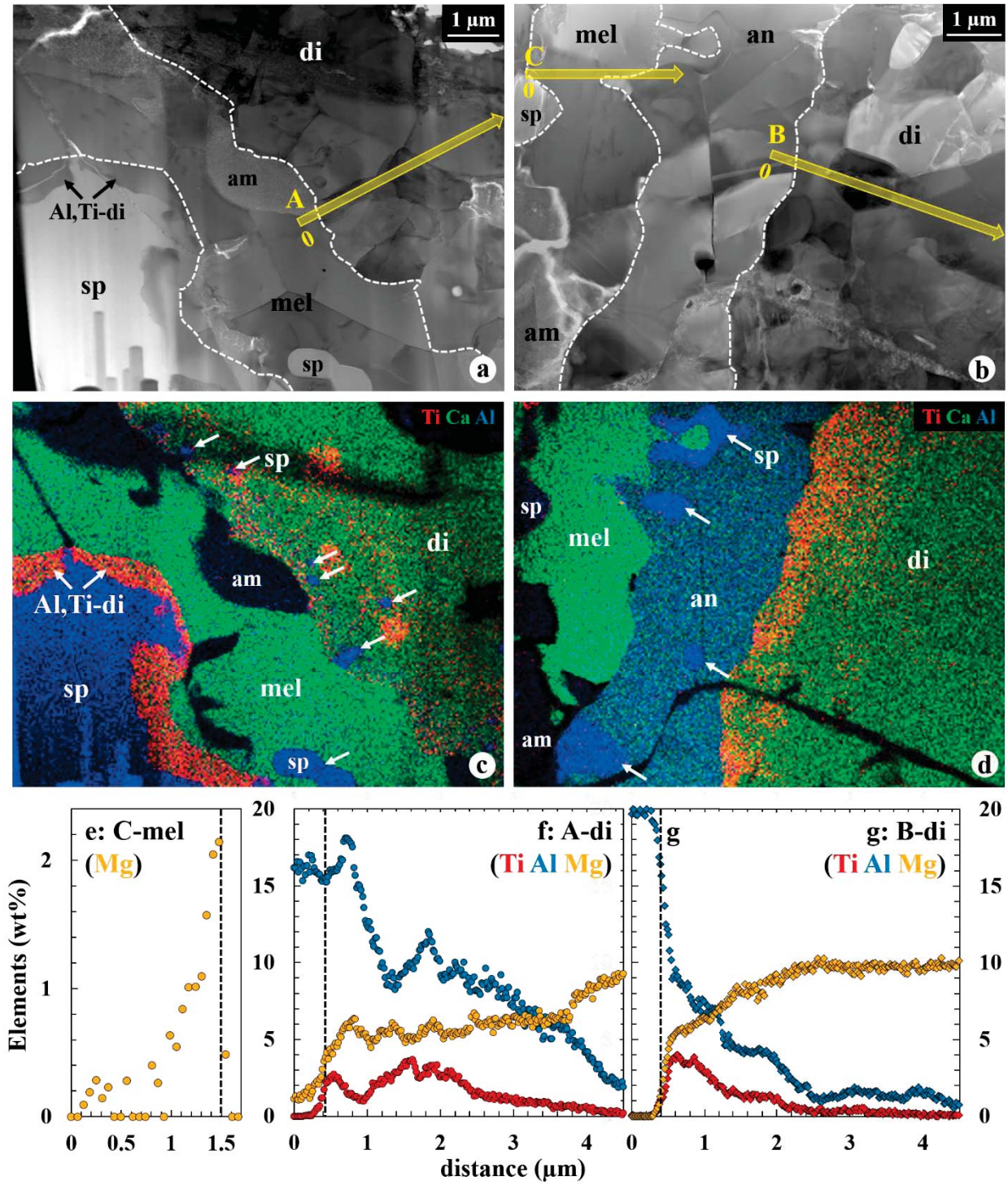


**Figure 6.** BF STEM images (a, b) and combined X-ray elemental map (c) in Mg (red), Ca (green), and Si (blue) of symplectic diopside-forsterite intergrowths in the outermost diopside layer.

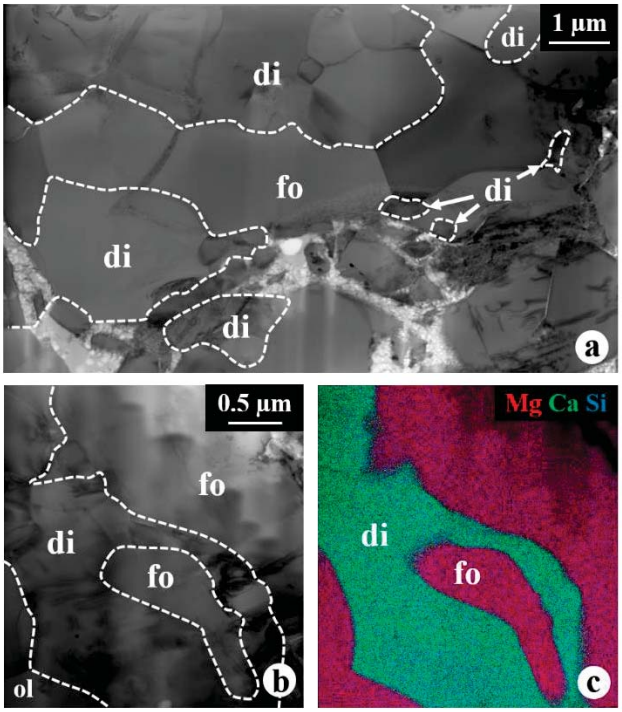


**Figure 7.** Oxygen isotopic compositions of individual minerals from the Vigarano CAI *Big Guy*. The data are plotted on an oxygen three-isotope diagram ($\delta^{17}O$ vs. $\delta^{18}O$) in (a) and as deviations from the terrestrial fractionation line ($\Delta^{17}O$) in (b). The terrestrial fractionation (TF) and carbonaceous chondrite anhydrous mineral (CCAM) lines are shown for reference.

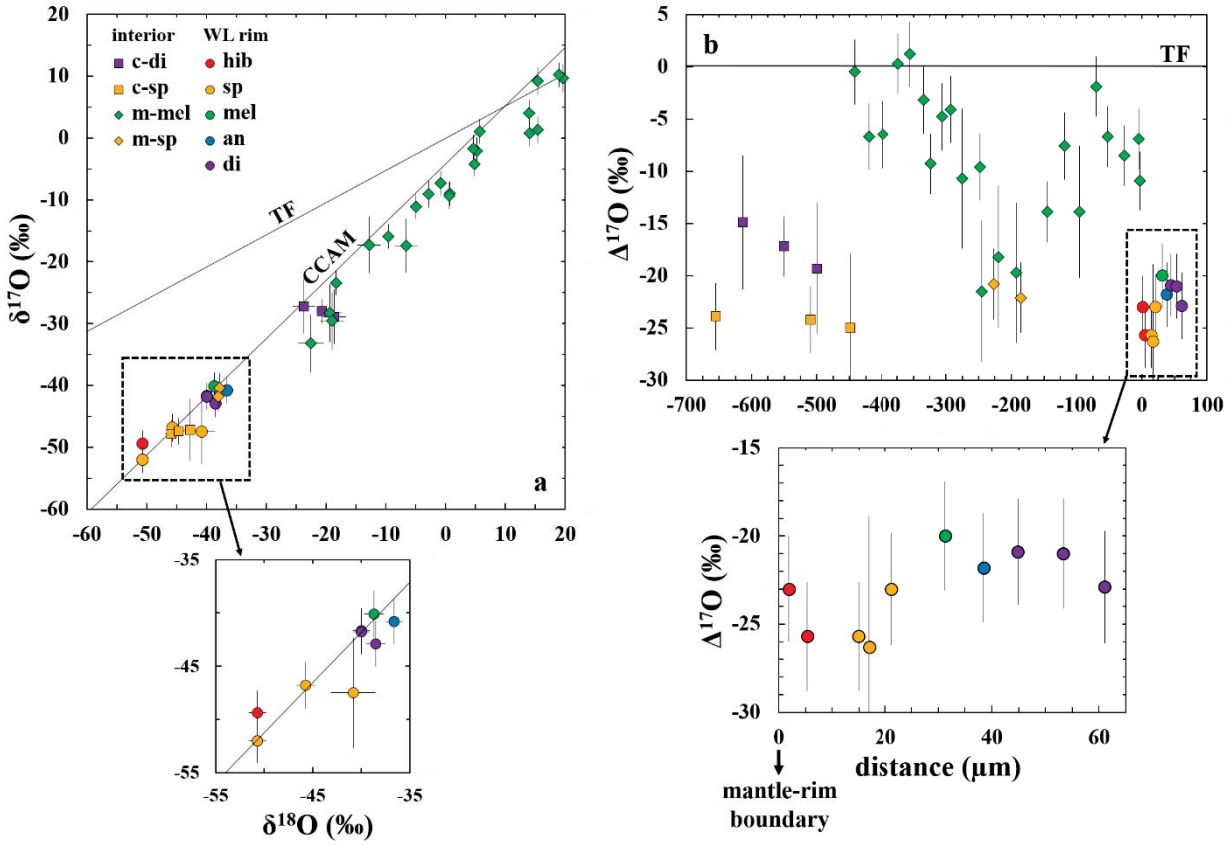


**Figure 8**. Magnesium isotopic compositions of individual minerals from the Vigarano CAI *Big Guy*. The data are plotted on diagrams of $\Delta^{26}Mg^*$ vs. $^{27}Al/^{24}Mg$. (a) Multicollection data of hibonite, spinel, and diopside. Regression through the data yields a slope corresponding to $(^{26}Al/^{27}Al)_0 = (4.94 \pm 0.12) \times 10^{-5}$ ($\chi^2 = 1.8$) and an intercept of $\Delta^{26}Mg_0^* = 0.09 \pm 0.04$‰ (errors are 2σ). (b) Monocollection data of melilite from the CAI mantle. Most of the melilite data points are plotted along with the high-precision isochron having $(^{26}Al/^{27}Al)_0 = 4.9 \times 10^{-5}$.

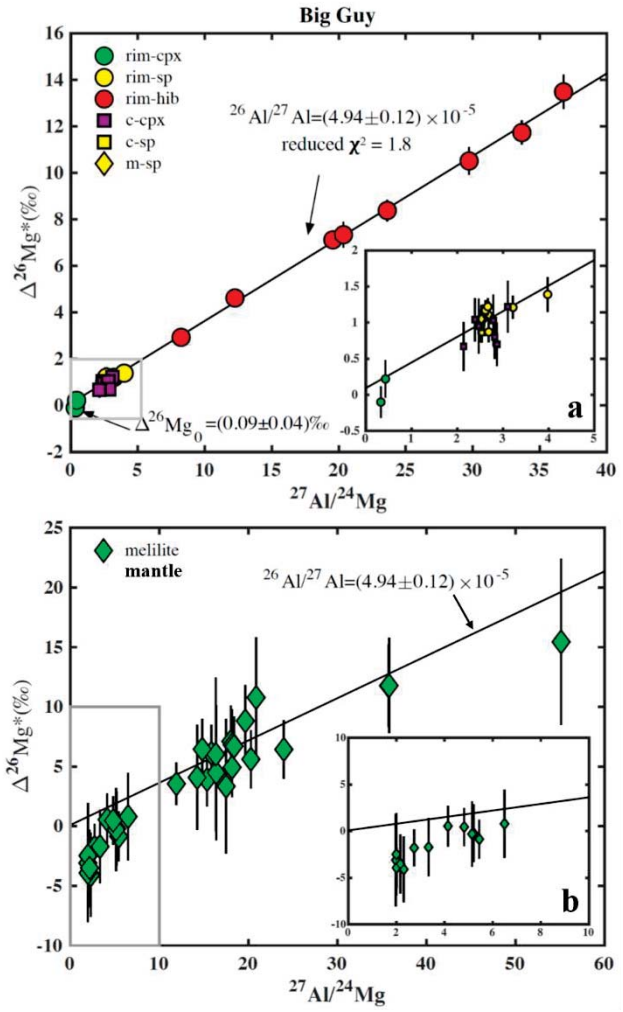


**Figure 9**. Siderophile element concentrations in RMNs enclosed by hibonite and melilite measured using TEM EDX. The abundances are normalized relative to CI chondrites, plotted in order of increasing volatility. Two RMNs are enriched in refractory siderophiles by factors of $10^4$-$10^5$ relative to CI chondrites, but show negative Mo anomalies.

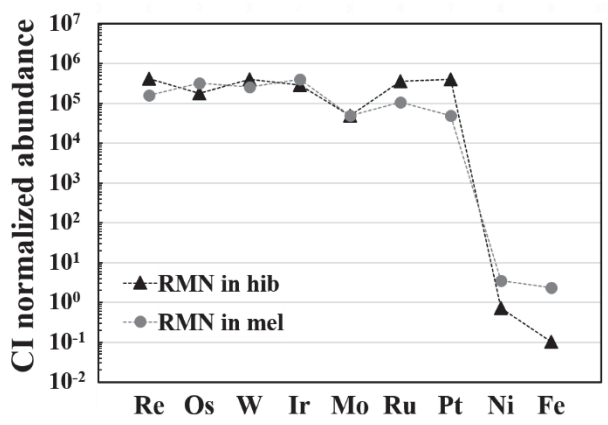


**Figure 10.** Schematic scenario for the WL rim formation on the Vigarano CAI *Big Guy*. The formation sequence of the WL rim is described as follows: (0) formation of the host CAI; (1) formation of a Ca,Al-rich melt layer by flash heating and extensive evaporation of Mg, Si, and possibly Ca; (2) crystallization of gehlenite, hibonite, and rare grossite; (3) sequential gas-solid reactions to form spinel, perovskite, melilite, diopside, and forsterite; and (4) parital replacement of melilite and Al-diopside by anorthite.

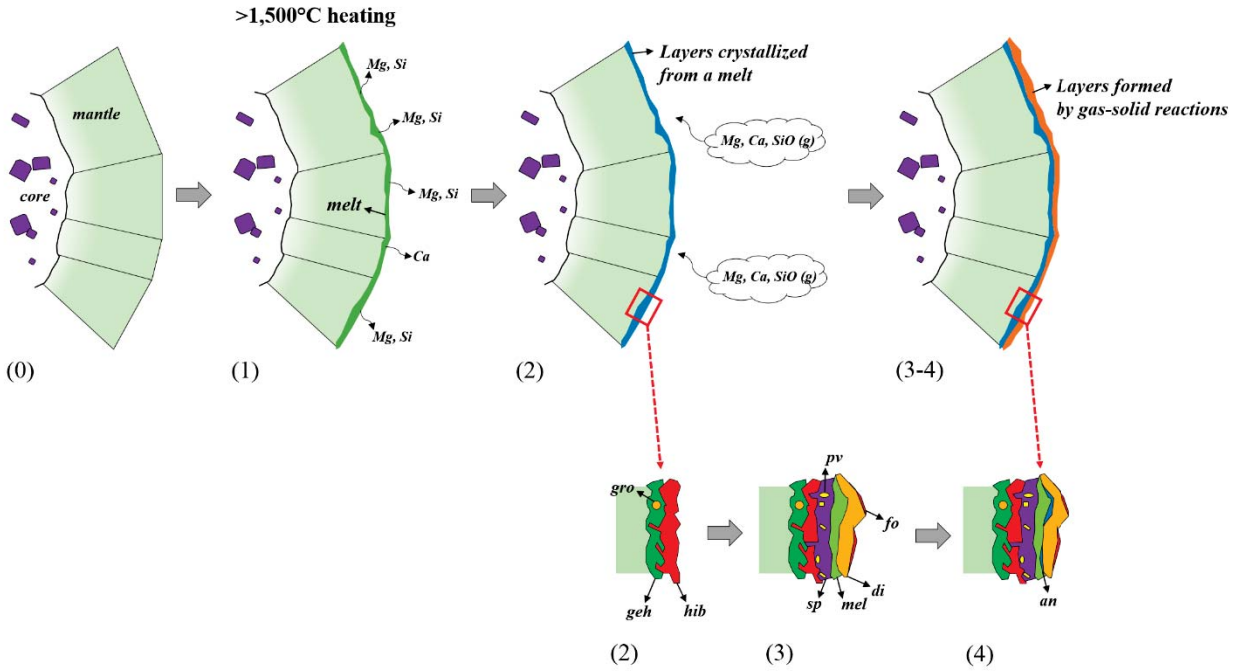

# Electronic Appendix A. Supplementary Material

Title: A Coordinated Microstructural and Isotopic Study of a Wark-Lovering Rim on a Vigarano CAI

Authors: Jangmi Han, Lindsay P. Keller, Ming-Chang Liu, Andrew W. Needham, Andreas T. Hertwig, Scott Messenger, Justin I. Simon

**Table EA1.** Relative sensitivity factors determined on standards with known $^{27}Al/^{24}Mg$ for this study (errors 2σ).

| | Burma Spinel | Madagascar hibonite | Pyroxene glass | Anorthite | Melilite glass |
|---|---|---|---|---|---|
| RSF | 1.37±0.01 | 1.34±0.02 | 1.25±0.01 | 1.20±0.04 | 1.00±0.01 |

**Figure EA1.** BSE images of the WL rim on the Vigarano CAI *Big Guy*. Locations of FIB sections are indicated. Abbreviations hereafter: hib = hibonite; pv = perovskite; sp = spinel; mel = melilite; an = anorthite; di = diopside; fo = forsterite.

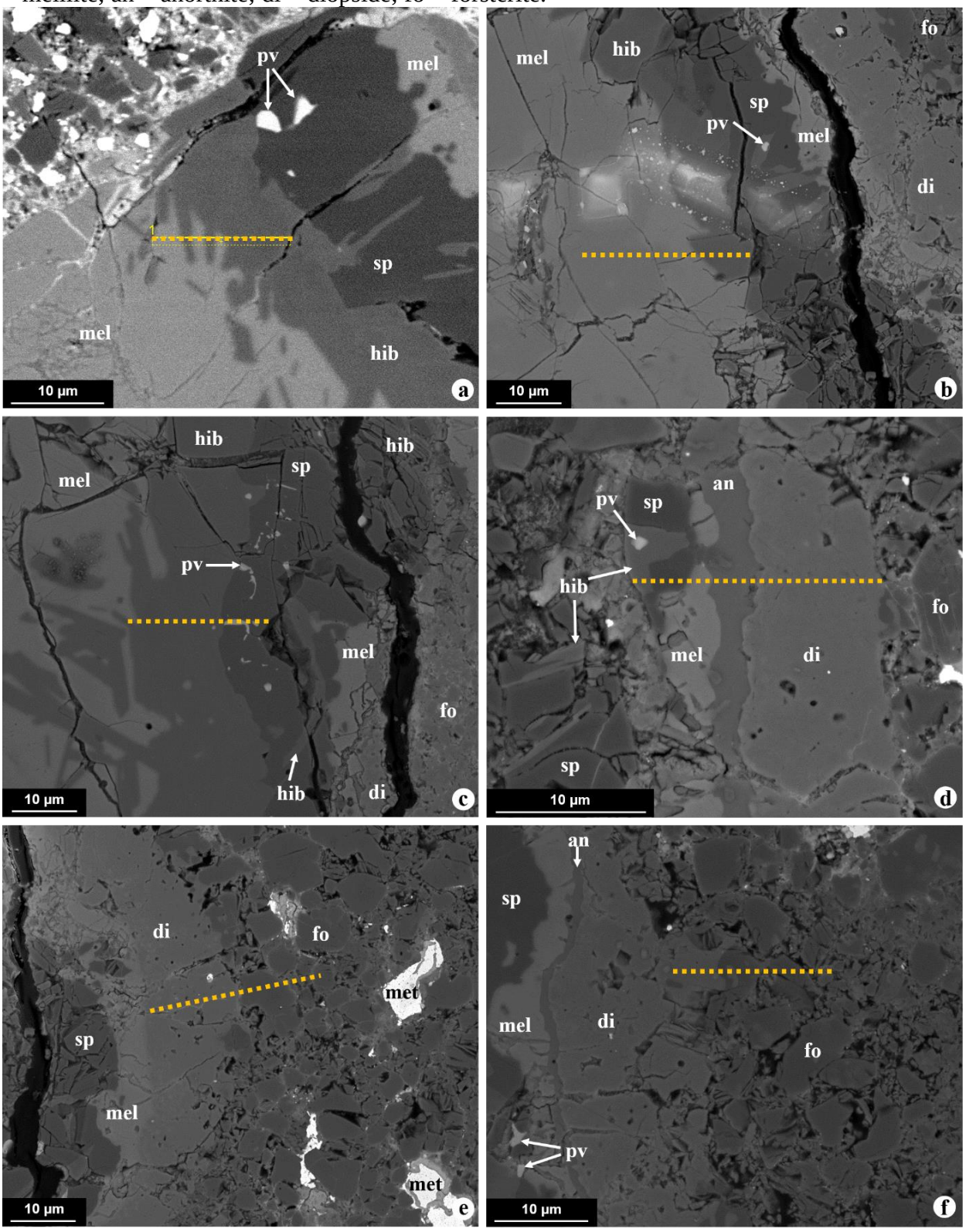

**Figure EA2.** BSE images of the WL rim on the Vigarano CAI *Big Guy*. Locations of NanoSIMS spots are indicated as red rectangles, whereas those of ims-1290 ion microprobe spots are indicated as yellow circles.

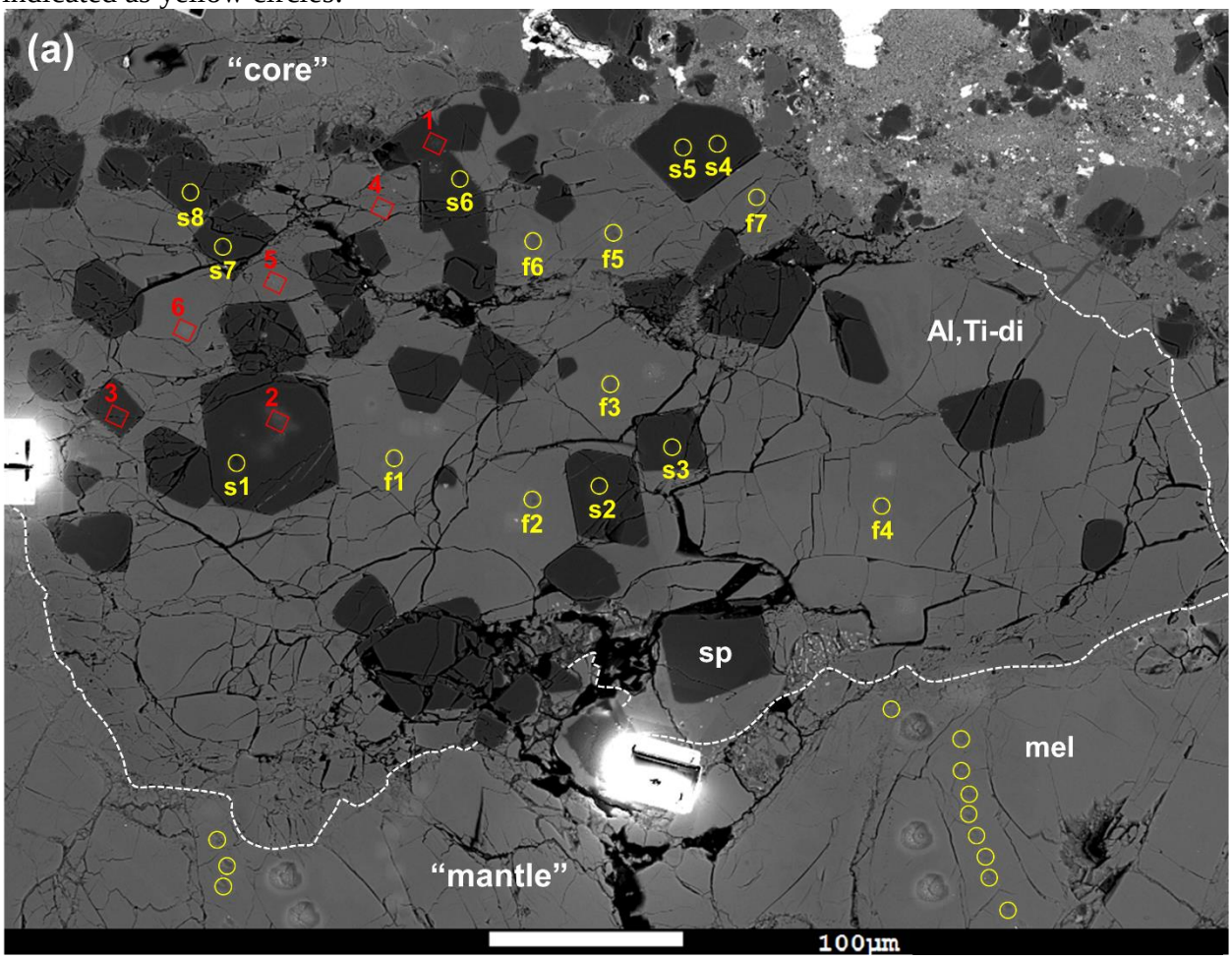

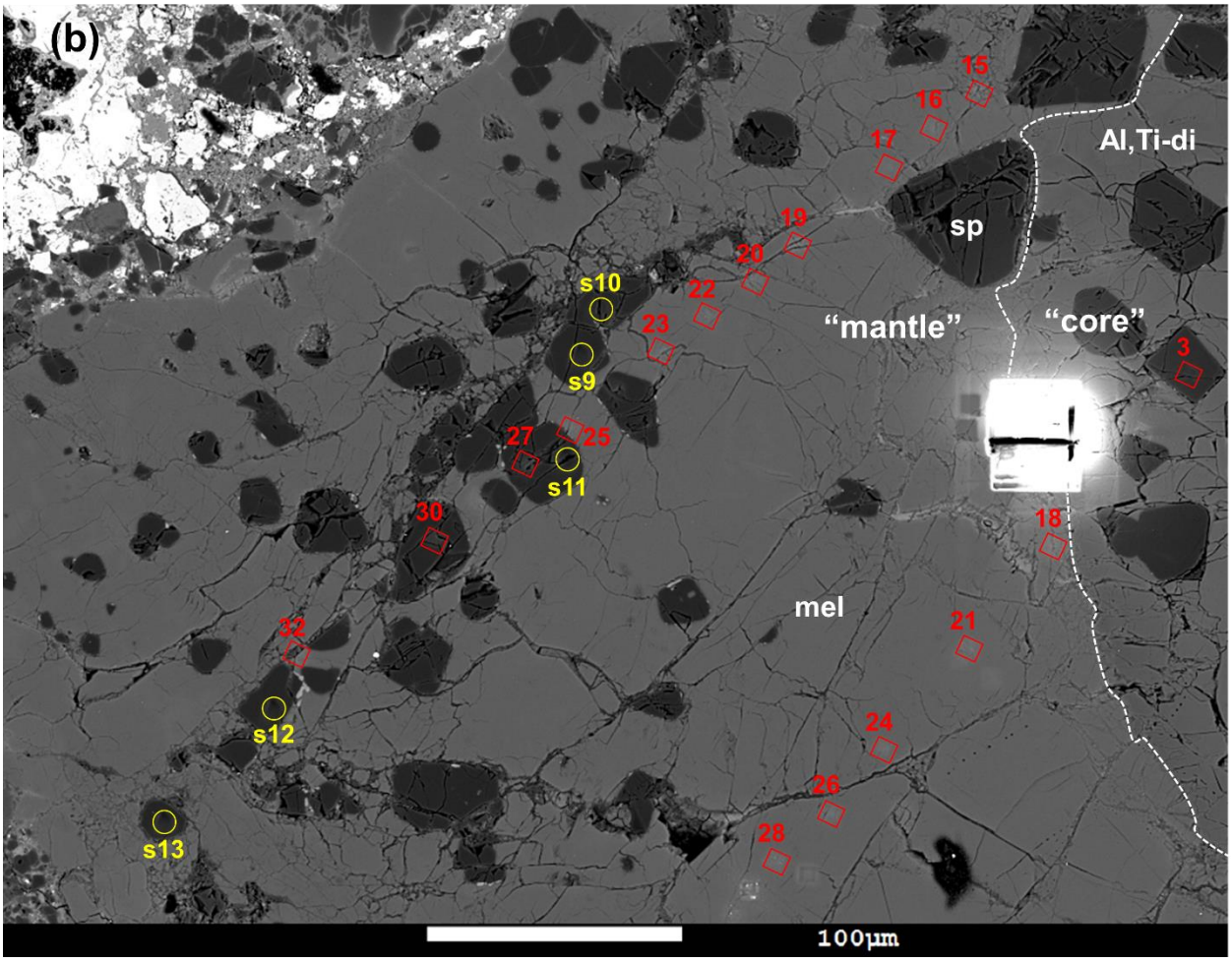
(b)
15
16
17
Al,Ti-di
sp
19
20
s10
22
23
"mantle"
"core"
3
s9
27
25
s11
30
18
mel
21
32
s12
24
26
s13
28
100µm

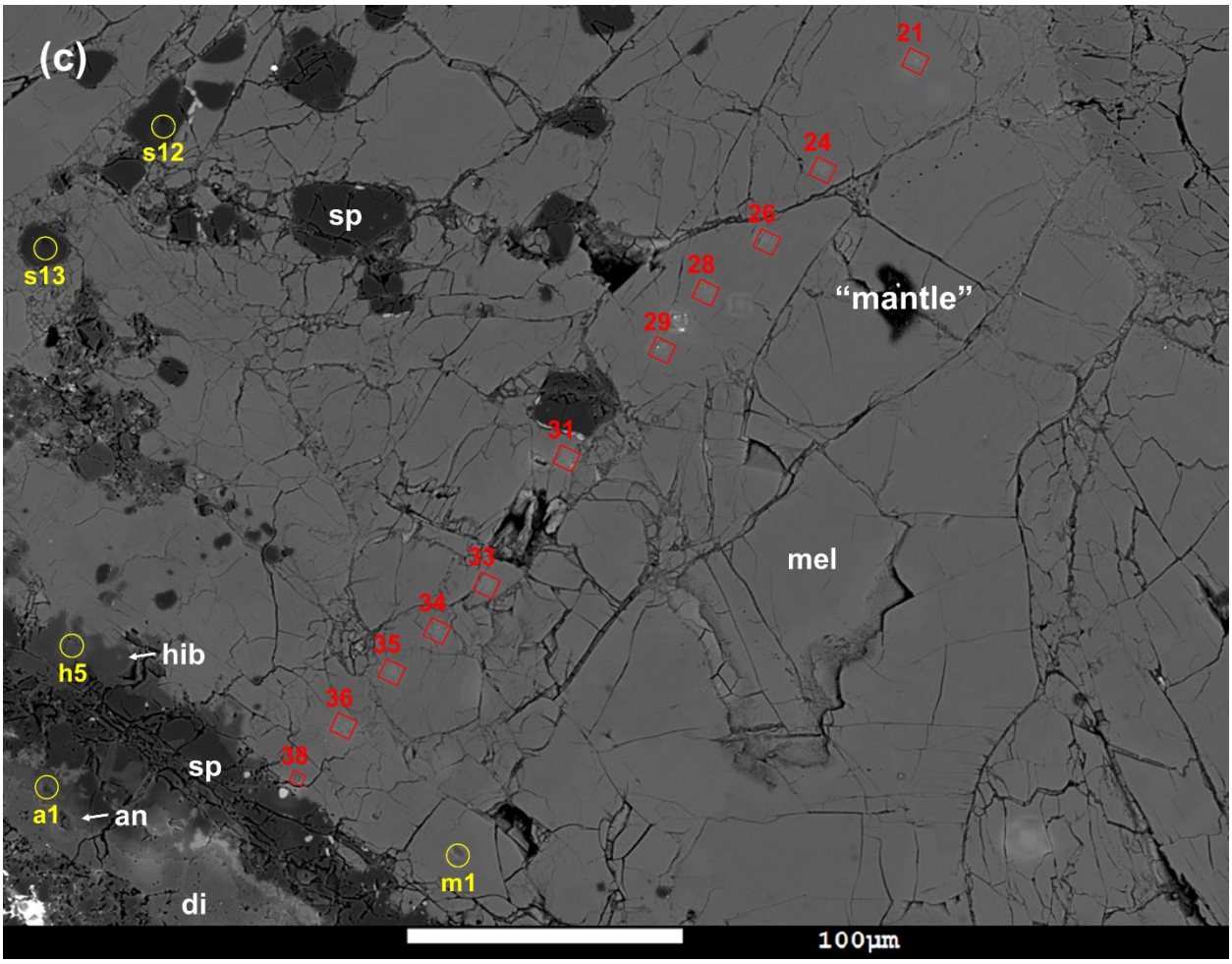
(c)
s12
sp
s13
21
24
26
28
29
"mantle"
31
mel
33
34
35
h5
hib
36
38
sp
a1
an
m1
di
100µm

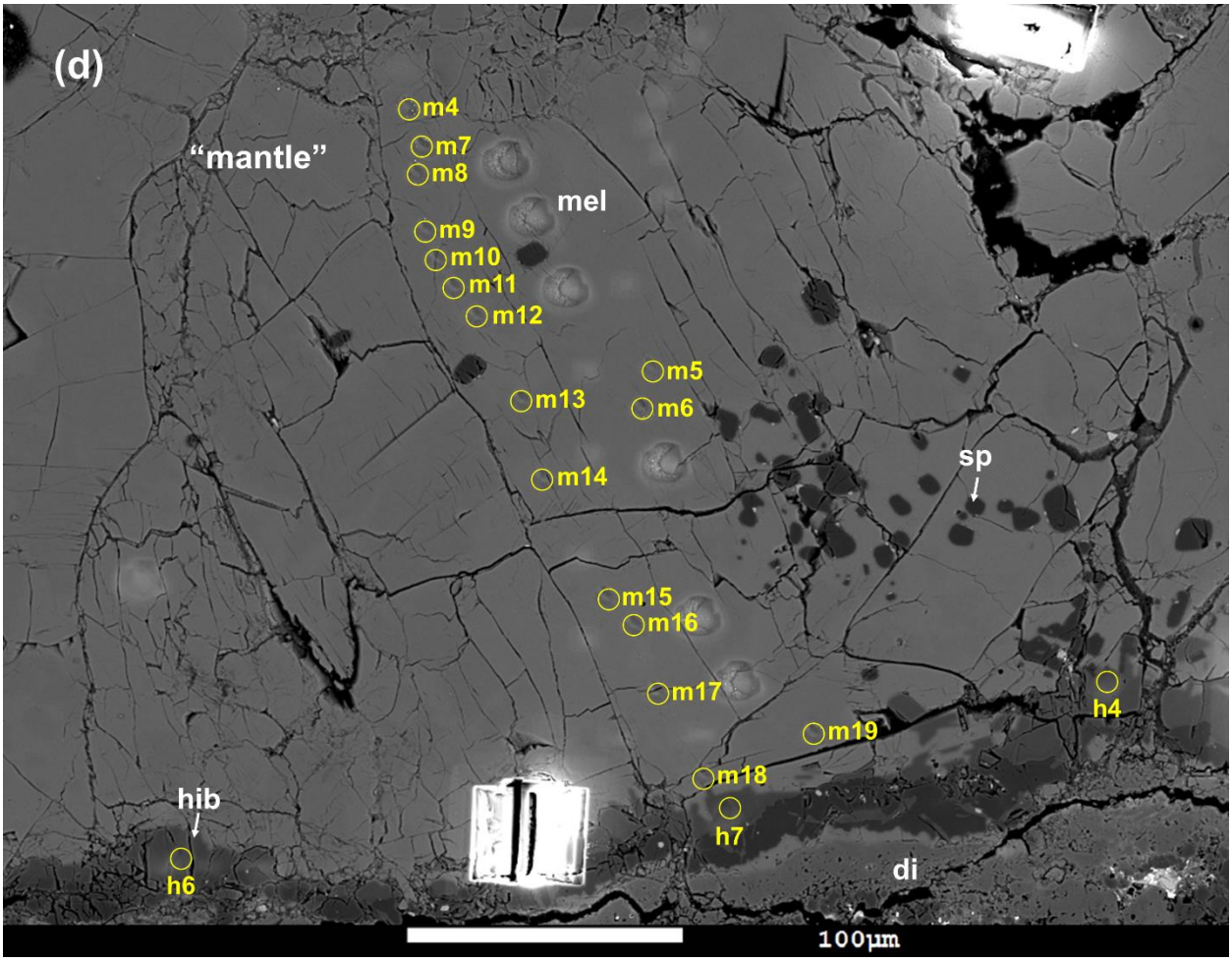
(d)
"mantle"
m4
m7
m8
mel
m9
m10
m11
m12
m5
m13
m6
sp
m14
m15
m16
m17
h4
m19
m18
hib
h7
h6
di
100µm

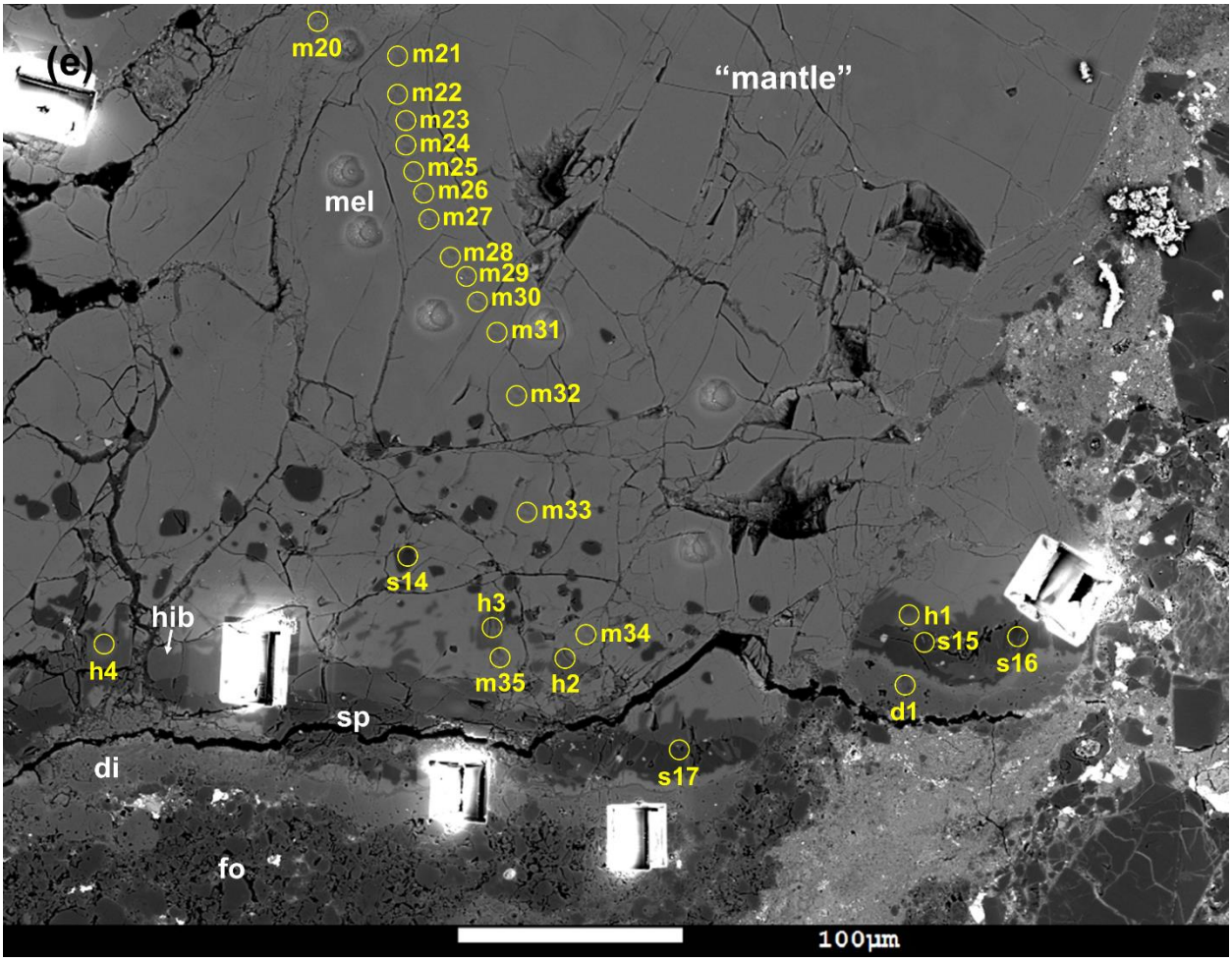
(e)
m20
m21
m22
m23
m24
m25
m26
m27
m28
m29
m30
m31
m32
m33
s14
h3
m34
m35
h2
h4
hib
sp
di
fo
s17
h1
s15
s16
d1
"mantle"
mel
100µm

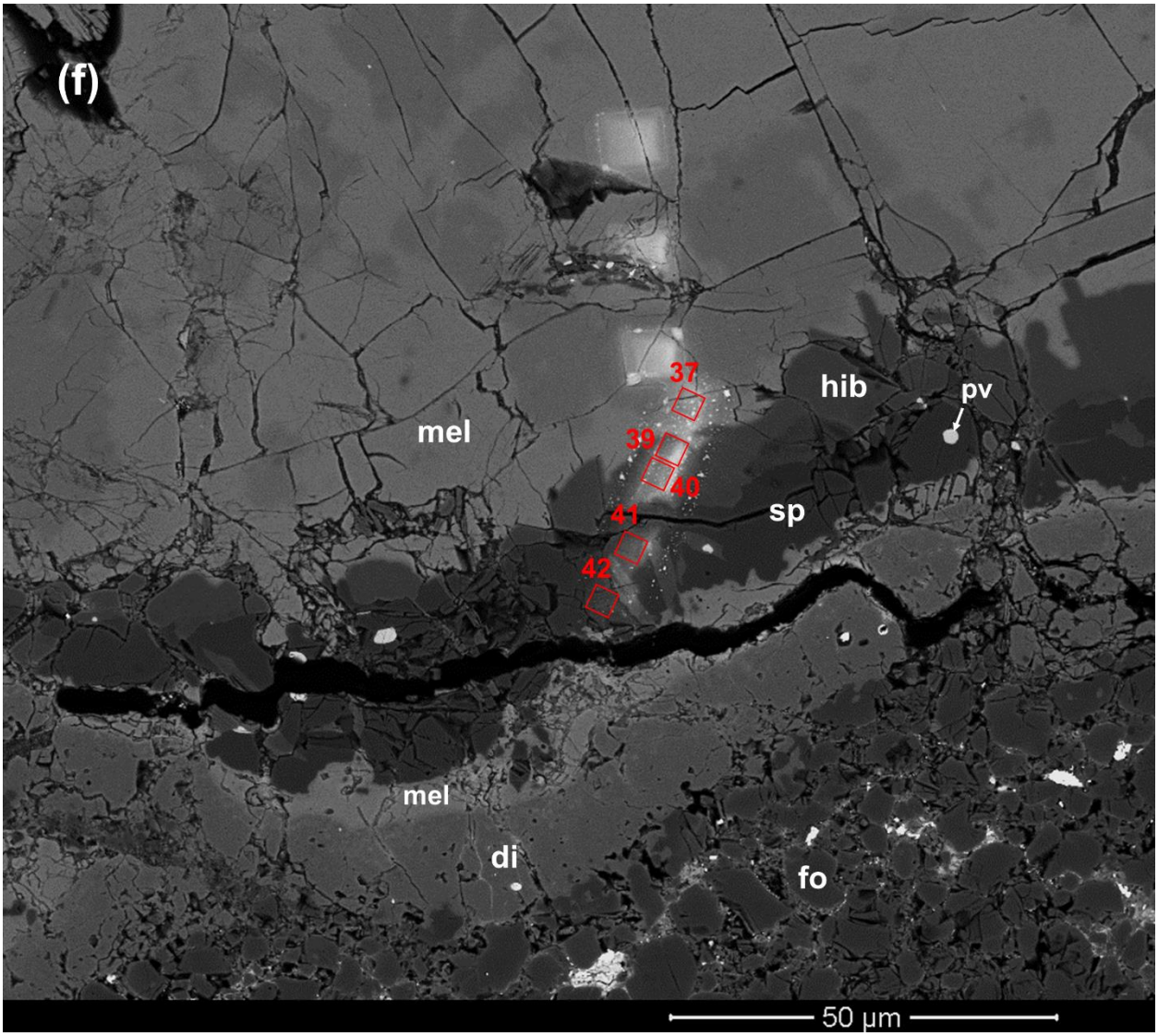
(f)
37
39
40
41
42
mel
hib
pv
sp
mel
di
fo
50 µm

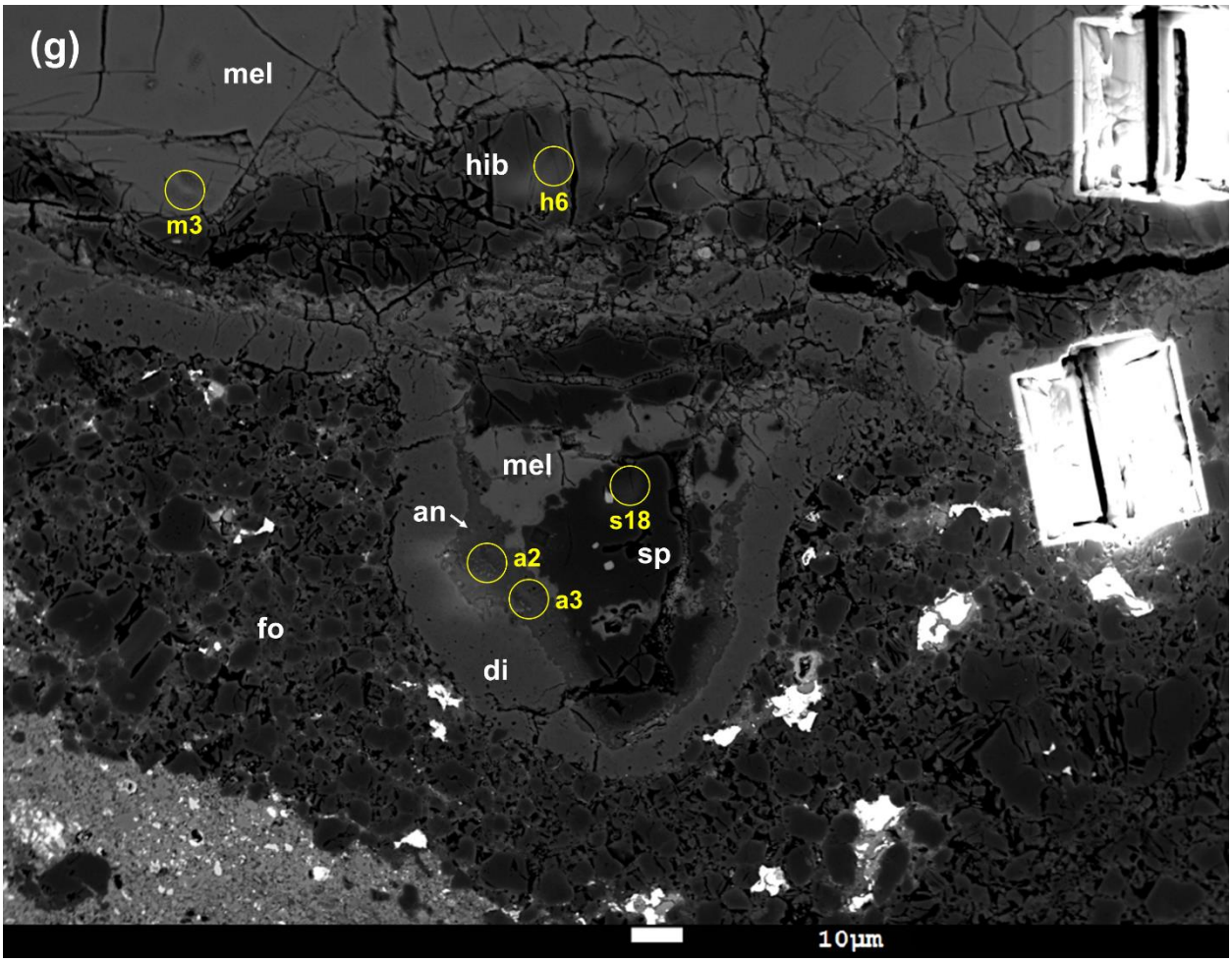
(g)
mel
hib
h6
m3
mel
an
s18
sp
a2
a3
fo
di
10µm

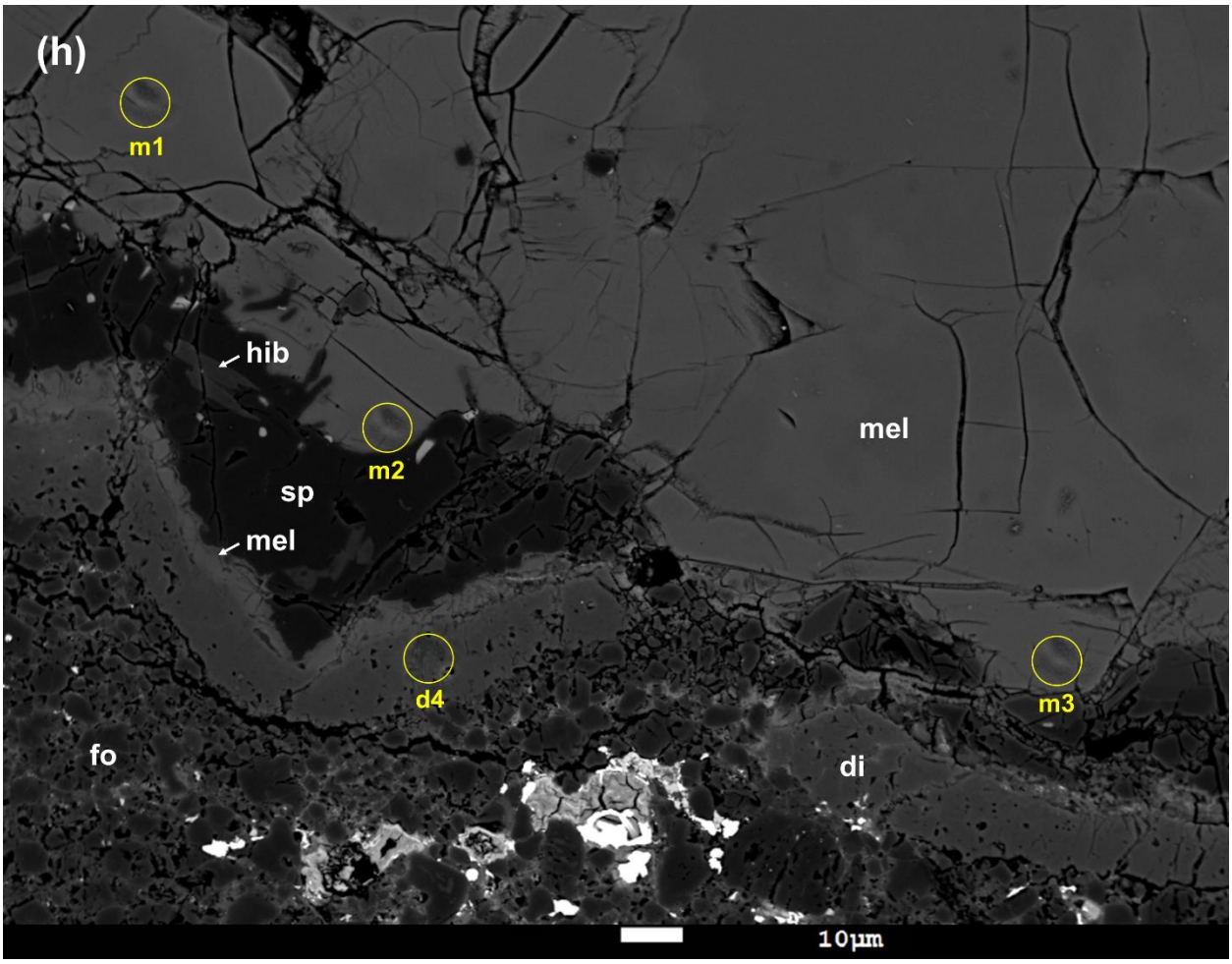
(h)
m1
hib
m2
sp
mel
mel
d4
m3
fo
di
10μm